An FDD-based modal parameter-less proportional flexibility-resembling matrix for response-only damage detection

Journal of Civil Structural Health Monitoring (2024) 14:401–429
https://doi.org/10.1007/s13349-023-00716-2

ORIGINAL PAPER

An FDD-based modal parameter-less proportional flexibility-resembling matrix for response-only damage detection

Andrea Calidori[1] · Giacomo Bernagozzi[2] · Silvia Castellaro[3] · Luca Landi[2] · Pier Paolo Diotallevi[2]

Received: 22 September 2022 / Accepted: 3 October 2023 / Published online: 15 November 2023

Abstract
Modal flexibility-based methods are effective tools for vibration-based structural damage detection, including in the output-only case. These methods are typically characterized by two stages: first, the modal parameters are identified, thus obtaining a certain number of modes; second, these modal parameters are used to assemble the modal flexibility matrix. This paper proposes a method for estimating a matrix that approximates a proportional flexibility matrix, termed proportional flexibility-resembling (PFR) matrix, and shows that this matrix can be used for damage detection and localization purposes. This matrix is obtained through signal processing operations to be executed after applying the first steps of the frequency-domain decomposition (FDD) technique—i.e., after the singular value decomposition of the spectral density matrix. The defining aspect of the PFR matrix is that, differently from the traditional formulation of modal flexibility and proportional flexibility matrices, it can be assembled without the need of an explicit identification of the modal parameters. In fact, the matrix is estimated by processing all first singular vectors and also all first singular values in a selected frequency range. In the proposed method, the typical two stage approach of traditional modal flexibility methods is avoided, and the intervention of an operator is limited to setting the values of a few parameters in the initial phase of the process. Numerical simulations and experimental data from a testbed structure were used to show the effectiveness of the proposed approach, and the analyses were performed by considering structures with different damage scenarios and damping properties.

Keywords Structural health monitoring · Damage detection · Modal flexibility · Output-only modal identification · Frequency-domain decomposition

1 Introduction

The applications of dynamic monitoring to civil engineering structures, like bridges and buildings, are rapidly spreading, and they are currently complementing the more traditional applications based on static monitoring. Typically, the ambient vibration responses due to unmeasured inputs, such as microtremors from the ground, wind or traffic loads, are measured, and the analysis of the recorded data is carried out in the so-called output-only conditions [1, 2]. One of the main objectives of this type of applications is to track relevant parameters over time to detect eventual changes which could be associated with structural degradation and damage [3]. These monitoring approaches and techniques could be applied not only to civil engineering structures, but also to aerospace structures and large mechanical systems [3, 4].

Among the different techniques for vibration-based damage detection, the most used methods are the ones based on modal parameters or based on quantities derived from the modal parameters themselves [3]. Thus, for structures monitored under ambient vibrations, the output-only modal identification techniques [1, 2] typically play a major role. The identification can be performed either in time domain or in frequency domain. The main advantage of frequency-domain methods is that a "natural modal decomposition" emerges in the frequency band where a mode dominates with respect to the other modes [1]. One of the simplest

✉ Giacomo Bernagozzi
giacomo.bernagozzi2@unibo.it

[1] Department of Structural, Geotechnical and Building Engineering, Politecnico di Torino, Corso Duca Degli Abruzzi 24, 10129 Turin, Italy

[2] Department DICAM, University of Bologna, Viale del Risorgimento 2, 40136 Bologna, Italy

[3] Department of Physics and Astronomy "Augusto Righi", University of Bologna, Viale Berti Pichat 8, 40127 Bologna, Italy

frequency-domain techniques is the basic frequency domain (BFD) approach, also known as peak picking technique. This technique is more user friendly and simpler to use than time domain methods [4]. A more advanced method is the frequency-domain decomposition (FDD) technique [4, 5]. This method preserves the user friendliness, and all information related to the different spectral density functions are condensed in one single plot, which is the plot of the singular values computed from the spectral density matrix [1]. In general, the FDD method is one of the most widely used methods for output-only modal identification. Other existing techniques for vibration-based damage identification are nonparametric techniques, such as the ones presented in [6–9].

The damage types that are typically detected using vibration-based techniques are those associated with a reduction in the stiffness of the structural elements being monitored, and effective techniques are those based on the estimation of the modal flexibility (MF) [10–31]. In these approaches a sort of a "modal synthesis" is performed, since the modal parameters (in terms of natural frequencies and mode shapes) are combined to obtain an estimate, from dynamic measurements, of the static flexibility matrix of the structure. The modal flexibility matrix can be directly used for damage detection and localization [10]. Alternatively, a more convenient approach is to apply some virtual inspection loads to the experimentally-derived modal flexibility model and use the estimated deflections for the condition assessment. In this way, all information of the modal flexibility matrix is condensed in a deflection vector, which can then be used to estimate the damage-sensitive features that are most appropriate for the considered structural typologies [11]. These deflection-based methods have been specifically developed and applied for different types of structures, including for example bridges [12–14] or buildings [11, 15–17].

The modal flexibility is based on cumulating the contribution from the different modes, and an important feature of the modal flexibility matrix is that it generally converges to an accurate solution using only the first few modes [10]. In any case, the modal truncation effects (even if small) are effects to deal with and effects that are expected whenever the modal flexibility matrix is estimated from an experimental test. Moreover, in the traditional formulation of the modal flexibility, derived from structural dynamics, mass-normalized mode shapes are required. However, in the context of output-only vibration tests with unmeasured inputs, the modal identification only provides arbitrarily-scaled mode shapes, and thus in this context the traditional formulation of the modal flexibility is not readily applicable [18].

Most of the research related to the modal flexibility-based methods has thus addressed the above-mentioned features, and limitations, and modifications to the traditional formulation of the modal flexibility have been proposed in the literature. In many cases even approximate techniques for estimating the modal flexibility have been accepted in literature, in favor of a wider applicability of the technique with a limited number of identified modes and in the context of output-only vibration tests.

In [19] a generalized flexibility matrix has been proposed, and, compared to the traditional formulation of the modal flexibility, the effect of truncating high-order modes can be considerably reduced with the proposed generalized approach. In [20] approaches have been proposed to predict and to reduce the truncation effects on the modal flexibility-based deflections. In the works [13, 14] the concept of the pseudomodal flexibility was introduced, leading to the applicability of the modal flexibility in the context of output-only dynamic tests. According to the mentioned works, the pseudomodal flexibility is estimated by assigning a unit scaling to each mode. The approaches presented in [16–18, 21, 22] aim at estimating a flexibility matrix that is proportional to the corresponding true matrix, which is termed as Proportional Flexibility Matrix (PFM). The underlying idea behind the mentioned approaches is to extract information about the mass distribution and/or about the mass normalization factors directly from the arbitrarily-scaled mode shapes, identified from an output-only test. As shown in [17], the higher the number of identified modes, the more accurate are the obtained estimates. In [23] the mode shapes, to be used for assembling the modal flexibility matrix, are estimated as the singular vectors computed from the decomposition of the acceleration response matrix measured for the considered structural system. Damage detection techniques based on the use of the modal flexibility are also applicable starting from dynamic strain measurements, as shown, for example, in [24–26].

All the mentioned approaches related to the use of the modal flexibility are typically characterized by two stages: first, the modal parameters, in terms of natural frequencies and mode shapes, are identified, thus obtaining a certain number of modes; second, these modal parameters are used to assemble the modal flexibility matrix. The search for an alternative approach that do not require an explicit identification of the modal parameters is the main reason that motivated the present study.

This paper proposes a vibration-based method for estimating a matrix that approximates a proportional flexibility matrix, hereinafter referred to as proportional flexibility-resembling (PFR) matrix. This matrix is estimated through signal processing operations to be performed after applying the first steps of the frequency-domain decomposition technique—i.e., after the singular value decomposition (SVD) of the spectral density matrix. The defining aspect of the proportional flexibility-resembling matrix is that it can be assembled without the need of an explicit identification of the modal parameters of the structure. This PFR matrix can

then be used for damage detection and localization purposes. In the method proposed for estimating the PFR matrix the typical two stage approach of traditional modal flexibility methods is avoided, and the intervention of an operator is limited to setting the values of a few parameters in the initial phase of the process. These few parameters are solely related to data acquisition and to the selection of the frequency range of interest.

The paper is organized as follows: Sect. 2 introduces the necessary theoretical background and an overview of how modal flexibility matrices can be estimated from vibration data. Section 3 presents the proposed method for estimating the PFR matrix, while Sect. 4 shows how such a matrix can be used for damage detection and localization purposes. The basic principles behind the estimation of the PFR matrix are explained in Sect. 5, while Sect. 6 shows how the procedure for PFR matrix estimation was derived and calibrated. Section 7 proves that the PFR matrix can be effectively used for damage detection, and this is shown through both numerical simulations (Sect. 7.1) and using experimental data from a testbed structure (Sect. 7.2).

2 Theoretical background

The modal flexibility matrix of a multi degree-of-freedom (MDOF) structure can be estimated from modal parameters, identified from a vibration test, as follows [18, 22, 27]:

$$\boldsymbol{F_p} = \boldsymbol{\Phi_p}\boldsymbol{\Lambda_p}^{-1}\boldsymbol{\Phi_p}^T \tag{1}$$

where $\Phi_p = [\phi_1, \phi_2, \ldots, \phi_p]$ is the $R \times$ p modal matrix holding the mass-normalized mode shape vectors and $\boldsymbol{\Lambda_p} = \text{diag}(\omega_1^2, \omega_2^2, \ldots, \omega_p^2)$ is a $p \times p$ diagonal matrix holding the natural angular frequencies squared. In the previous expressions, R is the number of the DOFs measured on the structure and p is the number of the identified modes. The generic element of $\boldsymbol{F_p}$ is so expressed:

$$f_{p,jk} = \sum_{r=1}^{p} \frac{\phi_{jr}\phi_{kr}}{\omega_r^2} = \sum_{r=1}^{p} \frac{\psi_{jr}\psi_{kr}}{\mu_r\omega_r^2} \tag{2}$$

In Eq. (2), ϕ_{jr} and ϕ_{kr} are the j-th and k-th components of the mass-scaled r-th mode shape, ψ_{jr} and ψ_{kr} are the corresponding unscaled components. The term μ_r in Eq. (2) is the modal mass of mode r, which can be calculated as follows: $\mu_r = \boldsymbol{\psi}_r^T \boldsymbol{M} \boldsymbol{\psi}_r$, where $\boldsymbol{M}$ is the mass matrix of the structure. In practical tests, it is generally not possible to estimate all the modes of the structure, and using a limited number of modes in the calculation leads to the estimation of a truncated modal flexibility matrix (as the one shown in Eq. 1). In any case, this truncated matrix is typically a good approximation of the true flexibility of the structure, even when considering only few of the first lowest modes. This is because, as shown in Eq. (2), the contribution of each mode to the matrix is proportional to the term $1/\omega_r^2$.

To estimate the modal flexibility matrix from output-only vibration data, mode shape scaling techniques can be used [1], such as the added mass method [32] or by performing the scaling using a finite element model [33]. Other approaches, specifically related to the flexibility estimation from output-only data, are based on determining an unscaled flexibility matrix that differs from the true flexibility by an unknown scaling factor [16–18, 21]. Different strategies have been developed for assembling this proportional flexibility matrix, using the following generic expression:

$$\widehat{\boldsymbol{F}}_{\boldsymbol{p}} = \sum_{r=1}^{p} \frac{\boldsymbol{\psi}_r \boldsymbol{\psi}_r^T}{\zeta_r \omega_r^2} \tag{3}$$

where ζ_r is a mode shape normalization factor. According to [16, 17, 21], the distribution of the masses can be estimated from the data, and the mode shapes in Eq. (3) can be normalized by considering the estimated proportional mass matrix. According to [18], the factor ζ_r in Eq. (3) is the ratio between the modal mass of the r-th mode and the modal mass of the first mode.

As evident in Eqs. (1–3), each formulation of the modal flexibility matrix requires the estimation of the modal parameters, in terms of mode shapes and natural angular frequencies (Fig. 1a). If for instance the frequency domain decomposition method [4, 5] is applied, first a singular value decomposition of the power spectral density (PSD) matrix is performed, and then the above-mentioned modal parameters can be estimated as the first singular vectors and the frequencies that correspond to the peaks in the plot of the singular values (as outlined in Fig. 1b, c). The modal flexibility matrix can then be estimated as shown in this section. The search for an alternative approach is the main reason that motivated the present study. Specifically, as outlined in Fig. 1d, the initial research question was the following: is it possible, starting from frequency domain decomposition, to estimate a matrix akin to a proportional flexibility matrix using all first singular vectors and all first singular values in a selected frequency range and without the need of an explicit identification of the modal parameters of the structure?

3 Proposed method for estimating the proportional flexibility-resembling matrix

The method proposed in this paper for estimating a proportional flexibility-resembling matrix, without the need of an explicit identification of the modal parameters, is applicable

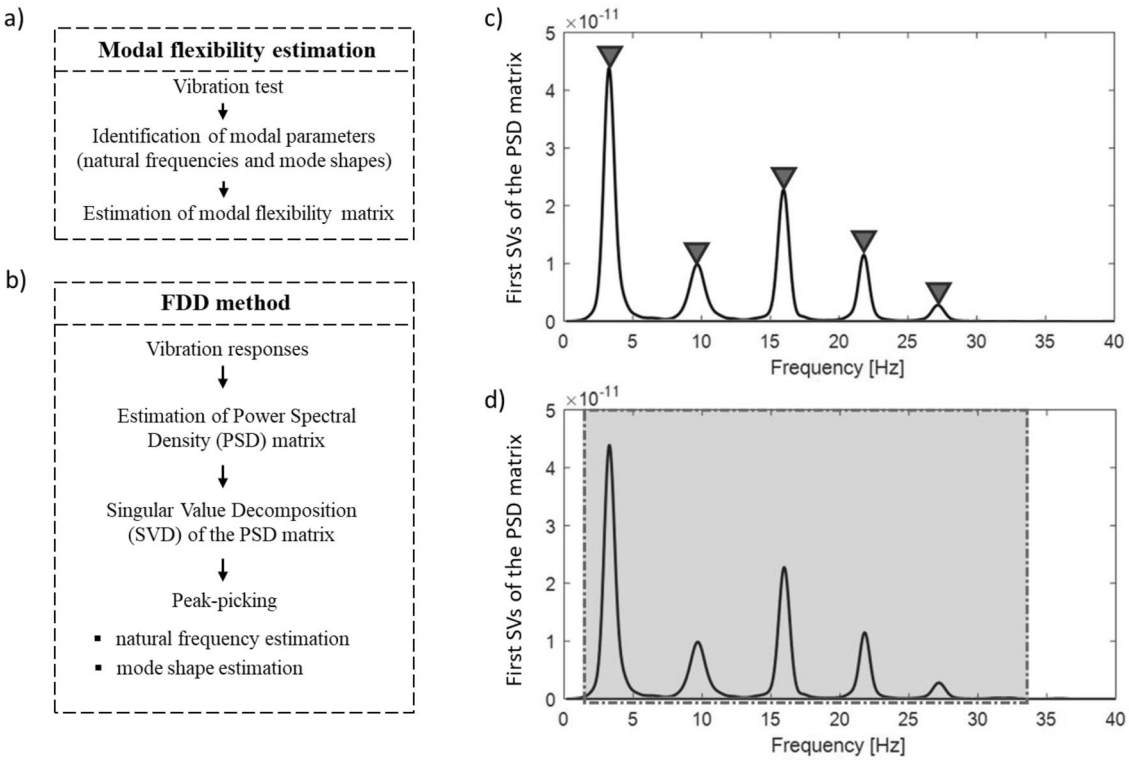

Fig. 1 Theoretical background: **a** main steps for modal flexibility estimation; **b** main steps of the FDD method for output-only modal identification; **c** a schematic exemplification of the peak-picking principle; **d** a schematic exemplification of the alternative approach of the proposed method that uses all the first singular values and singular vectors in a selected frequency range

starting from the output-only vibration responses of the structure and is based on signal processing operations to be performed after applying the first steps of the frequency domain decomposition technique [4, 5]. The defining equation of the proportional flexibility-resembling matrix and all the steps of the method for estimating this matrix are presented in this section. The proposed proportional flexibility-resembling matrix is a matrix that approximates a proportional flexibility matrix, as shown in Sect. 5 and through the numerical analyses of Sect. 6. The proposed method is formulated for structures that can be modeled as plane structures, whose structural behavior is analyzed in one direction, and that have a regular distribution of the masses.

Let us consider the displacement response time histories related to the DOFs measured on a structure tested under ambient vibrations (where the unmeasured inputs are assumed as white-noise excitations). Assuming that the length of the signal is $T = N\Delta t$ (where Δt is the sampling interval and N is the even total number of samples), the discrete-time sampled displacement vector is $\boldsymbol{y}(n\Delta t)$, where the signal vector has R components.

The first step of the proposed method implies to process the signal to calculate its power spectral density matrix $\boldsymbol{G}_y(n\Delta\omega)$, where $\Delta\omega$ is the angular frequency resolution, i.e., $\Delta\omega = \frac{2\pi}{N\Delta t}$, and n is the index related to the frequency bins. The next step is to perform a singular value decomposition of the PSD matrix, according to the frequency domain decomposition technique [4]:

$$\boldsymbol{G}_y(n\Delta\omega) = \boldsymbol{U}_n\boldsymbol{S}_n\boldsymbol{U}_n^H, n = 1 \ldots \frac{\mathrm{N}}{2} \tag{4}$$

where $\boldsymbol{G}_y(n\Delta\omega)$, $\boldsymbol{U}_n$ and $\boldsymbol{S}_n$ are $R \times R$ matrices which vary from frequency line to frequency line, and the superscript H denotes the conjugate (or Hermitian) transpose. In Eq. (4), $\boldsymbol{S}_n$ is a diagonal matrix holding the singular values, while $\boldsymbol{U}_n$ is a unitary matrix holding the singular vectors (i.e., $\boldsymbol{U}_n\boldsymbol{U}_n^H = \boldsymbol{I}$, where $\boldsymbol{I}$ is the identity matrix, thus the Euclidean norm of the singular vectors is equal to 1). It is implied that in the present method the DC values are excluded, as it can be observed in Eq. (4). In Eq. (4), the maximum value of the index n (i.e., $\frac{N}{2}$) is related to the Nyquist frequency. Of course, this frequency (and thus the sampling frequency) must be selected by ensuring that the significant modes of the structure are included in the established frequency range.

The first column of $\boldsymbol{U}_n$ is defined as the first singular vector $\boldsymbol{u}_{1n} = \boldsymbol{u}_1(n\Delta\omega)$ and can be assumed as the best fitting representation of the operational deflection shape (ODS) for the frequency $n\Delta\omega$. In general, singular vectors

have complex components: assuming that the structure is lightly and proportionally damped, it is possible to represent the ODSs as vectors $\boldsymbol{v_n}$ with real components according to the principles of the Standard Technique [34]. Thus, v_{jn} is the j-th component of vector $\boldsymbol{v_n}$ and is given by:

$$v_{jn} = \left|u_{1jn}\right| \bullet sgn\left(\Re(u_{1jn})\right) \tag{5}$$

Then, the $R \times \frac{\mathrm{N}}{2}$ matrix $\boldsymbol{V}$ is assembled, which is denoted as the matrix of the first singular vectors. The columns of such a matrix are the vectors $\boldsymbol{v_n}$, i.e.,

$$\boldsymbol{V} = \left[\boldsymbol{v}_1, \boldsymbol{v}_2, \ldots, \boldsymbol{v}_{N/2}\right] \tag{6}$$

In a similar way, the diagonal $\frac{N}{2} \times \frac{N}{2}$ matrix $\boldsymbol{Z_d}$ is determined, which is denoted as the matrix of the weighted first singular values, and which is defined as follows:

$$\boldsymbol{Z_d} = \mathrm{diag}\left(z_n\right) = \mathrm{diag}\left(\omega_n s_{dn}\right), \quad n = 1 \ldots \frac{\mathrm{N}}{2} \tag{7}$$

where $s_{dn} = s_d(n\Delta\omega)$ is the first singular value of the displacement power spectral density matrix for the n-th frequency line. For each frequency bin, the first singular values are modified by the value of the corresponding angular frequency ω_n, so to obtain the weighted first singular values z_n.

Based on the quantities defined in Eqs. (6,7), the proportional flexibility-resembling matrix $\boldsymbol{F}^*$ proposed in this paper is expressed as:

$$\boldsymbol{F}^* = \boldsymbol{V}\boldsymbol{Z_d}\boldsymbol{V}^T \tag{8}$$

Though the previous expressions derive from processing a displacement signal, the estimation process of $\boldsymbol{F}^*$ is also possible starting from a recorded velocity or acceleration signal. In fact, the displacement PSD matrix $\boldsymbol{G_y}(\omega)$ can be calculated by dividing the velocity PSD matrix $\boldsymbol{G_{\dot{y}}}(\omega)$ or the acceleration PSD matrix $\boldsymbol{G_{\ddot{y}}}(\omega)$ by specific powers of the angular frequency ω:

$$\boldsymbol{G_y}(\omega) = \frac{1}{\omega^2}\boldsymbol{G_{\dot{y}}}(\omega) = \frac{1}{\omega^4}\boldsymbol{G_{\ddot{y}}}(\omega) \tag{9}$$

It is worth noting that the division by these specific powers of the angular frequency affects the way in which the displacement, velocity and acceleration spectra appear, as already discussed in [35].

Since the singular vectors are always unit vectors, it can be proven that the only change in the singular value decomposition of $\boldsymbol{G_{\dot{y}}}(\omega)$ or $\boldsymbol{G_{\ddot{y}}}(\omega)$ and the SVD of $\boldsymbol{G_y}(\omega)$ resides in the singular values. Namely, the following equation expresses the relation between the first singular value of the displacement PSD matrix, $s_d(\omega)$, and its counterparts $s_v(\omega)$ and $s_a(\omega)$, i.e., the first singular value of the velocity and acceleration PSD matrices:

$$s_d(\omega) = \frac{s_v(\omega)}{\omega^2} = \frac{s_a(\omega)}{\omega^4} \tag{10}$$

While Eq. (9) is always true in analytical, noise-less, and continuous-time models, it must be noticed that it represents the frequency domain integrations of $\boldsymbol{G_{\dot{y}}}(\omega)$ and $\boldsymbol{G_{\ddot{y}}}(\omega)$, and so a high-pass filter is required to avoid the amplification of the noise that usually governs the signal for frequencies close to DC. To avoid the aforementioned noise amplification when using integrated forms of singular values, a discriminant function $\varepsilon_n = \varepsilon(n\Delta\omega)$ is introduced in the diagonal $\frac{\mathrm{N}}{2} \times \frac{\mathrm{N}}{2}$ matrix of the weighted first singular values, which takes this new expression:

$$\boldsymbol{Z} = \mathrm{diag}\left(z_n\varepsilon_n\right) = \mathrm{diag}\left(\frac{s_n\varepsilon_n}{\omega_n^c}\right), \quad n = 1 \ldots \frac{\mathrm{N}}{2} \tag{11}$$

In Eq. (11), $s_n = s(n\Delta\omega)$ is the first singular value of the PSD matrix (regardless of whether the vibrational output was recorded as a displacement, velocity, or acceleration signal); c is a coefficient that varies depending on the signal type, as it follows:

- $c = -1$ if $\boldsymbol{y}(n\Delta t)$ is a displacement signal;
- $c = 1$ if $\boldsymbol{y}(n\Delta t)$ is a velocity signal;
- $c = 3$ if $\boldsymbol{y}(n\Delta t)$ is an acceleration signal.

The calibration of the procedure used to weigh the first singular values through the corresponding angular frequencies represented a fundamental step in the definition of the PFR matrix, and Sect. 6 of the paper shows how such values of the coefficient c have been defined.

The introduced discriminant function ε_n must be determined by the operator in the initial phase of the process and through a first analysis of the data. The general formula is:

$$\varepsilon(n\Delta\omega) = \begin{cases} 0 & if \quad n < \hat{n} \\ 1 & if \quad n \geq \hat{n} \end{cases} \tag{12}$$

The parameter $\hat{n}$ is directly related to the cutoff frequency, which is $\hat{\omega} = \hat{n}\Delta\omega$. If $\boldsymbol{y}(n\Delta t)$ is a displacement signal, the parameter $\hat{n}$ is set to 1 and thus the cutoff frequency is equal to $\Delta\omega$ (in such a case, the discriminant function is substantially not altering the function of the weighted first singular values). Otherwise, if $\boldsymbol{y}(n\Delta t)$ is a velocity or acceleration signal, the cutoff frequency can be chosen as the frequency for which the weighted first singular value function $z_n = \frac{s_n}{\omega_n^c}$ presents the first minimum point, namely between the first descending branch of the curve and the first mode spectral bell, as shown in the example of Fig. 2.

Considering what stated above, the following equation can be considered as the generalized expression of the proportional flexibility-resembling matrix $\boldsymbol{F}^*$:

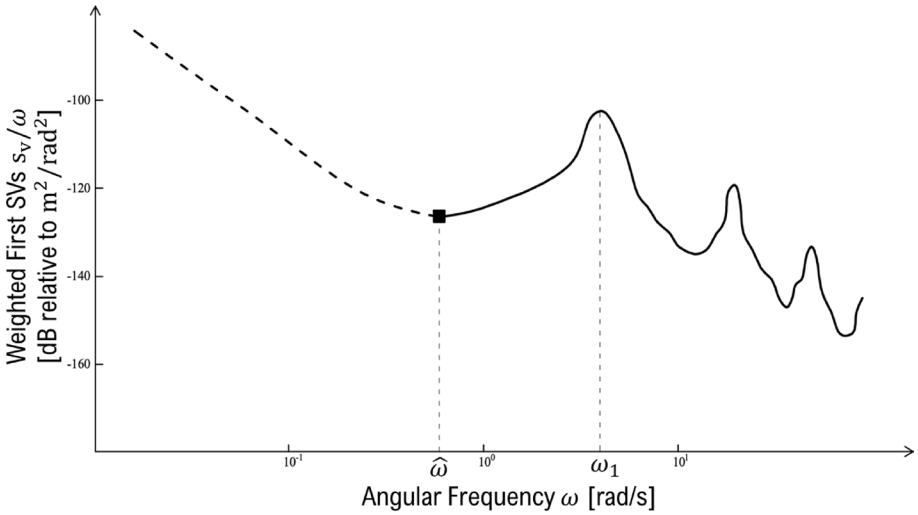

Fig. 2 Exemplification of a plot of weighted first singular values obtained from a velocity PSD (i.e., $s_v(\omega)/\omega$), with the indication of the chosen cutoff frequency $\widehat{\omega}$ and the first mode natural frequency ω_1

$$\boldsymbol{F}^* = \boldsymbol{V}\boldsymbol{Z}\boldsymbol{V}^T \tag{13}$$

It is worth noting that the PFR matrix that can be obtained from Eq. (13) for a velocity or acceleration signal with the use of the discriminant function is almost the same that can be estimated from Eq. (8) using a displacement signal. This is true especially for structures with a sufficiently high first modal frequency, such that the majority of the points of the first mode spectral bell are related to angular frequencies higher than 1 rad/s.

The generalized expression of $\boldsymbol{F}^*$ reported in Eq. (13) is characterized by a strong formal resemblance to the expression of the modal flexibility matrix expressed in Eq. (1): the modal matrix $\boldsymbol{\Phi_p}$ is replaced by the matrix of the first singular vectors $\boldsymbol{V}$, while the inverse of the matrix of the squared natural frequencies $\boldsymbol{\Lambda}$ is replaced by the matrix of the weighted first singular values $\boldsymbol{Z}$. However, while the modal flexibility matrix is assembled using the set of the identified modal parameters, the PFR matrix is constructed using all first singular vectors and all first singular values of the selected frequency range.

Lastly, it should be noted that a statistical approach is required to get a good estimation of the proportional flexibility-resembling matrix; namely, acquired data can be characterized by measurement errors and noise that can adversely affect the results. At the same time, the power of the input signal is rarely equally distributed at all the sampled frequencies during all the measurement time. These issues can be solved by segmenting the recorded signal $\boldsymbol{y}(n\Delta t)$ into a statistically relevant number ϑ of segments $\boldsymbol{y_k}(n\Delta t)$, and each segment should have the same length T_ϑ that is required for performing an output-only modal identification. According to [36], this length is typically taken in the following range:

$$T_\vartheta \approx [100 \dots 500]T_1 \tag{14}$$

where T_1 is the natural period of the first mode. Thus, the total length of the measurements required to estimate the proposed PFR matrix is equal to $T = \vartheta T_\vartheta$. Proceeding this way, it is possible to apply the aforementioned steps to each k-th segment and calculate the corresponding proportional flexibility-resembling matrix $\boldsymbol{F_k^*}$ through Eq. (13). In the end, the best estimate of $\boldsymbol{F}^*$ can be obtained as the average of the resulting $\boldsymbol{F_k^*}$ matrices:

$$\boldsymbol{F}^* = \frac{1}{\vartheta}\sum_{k=1}^{\vartheta} \boldsymbol{F_k^*} \tag{15}$$

Of course, the longer is T_ϑ and the higher is ϑ, the more accurate the estimate of the matrix $\boldsymbol{F}^*$ is.

4 Damage localization using the proposed PFR matrix

To show that the proposed PFR matrix can be used for damage detection purposes, existing flexibility-based damage detection methods have been considered, and the proposed PFR matrix has been used in place of the traditional modal flexibility matrix. Comparisons have also been made between the results obtained using the traditional modal flexibility matrix and the proposed PFR matrix, as shown in Sect. 7.1. One of the selected existing methods is the Positive Shear Inspection Load (PSIL) method [15]. The method is formulated for structures that can be modeled as shear building structures, and the considered damage-sensitive features are the interstory drifts (i.e., lateral interstory displacements) computed from

flexibility-based deflections. In the original formulation of the method [15] the modal flexibility is assembled from output-only data using an a-priori estimate of system mass matrix to perform the modal scaling; then, in [16, 17] it was shown that the method can also be applied using proportional flexibility matrices. A second existing method that was considered is the Positive Bending Inspection Load (PBIL) method [12]. This method was formulated for flexure-type beam-like structures. For those structures different damage-sensitive features can be estimated from the flexibility-based deflections. Among these DSFs, the most common approach is to adopt the curvature of the deflections [28, 29]. It is expected that the proposed PFR matrix could be used for damage detection in different types of structures using different strategies and damage-sensitive features, but this will be tested in future research.

The PSIL method for damage detection can be applied if horizontal vibration measurements are available at each story of the considered shear building structure. According to the method, the modal flexibility of the structure is estimated, and then to compute the deflections a positive shear inspection load is applied—i.e., a load such that the shear force is positive in each story and all the story displacements are induced in the same direction. Among the different PSIL loads that can be selected, in [15] it is suggested to use a set of unitary forces applied to each story—i.e., a load vector $\boldsymbol{b} = [1\ 1 \ldots 1]^T$ (Fig. 3a). The PBIL method is applicable starting from vibration measurements that are recorded in the direction that is orthogonal to the longitudinal axis of the beam. The virtual inspection load to be applied according to the method (i.e., the PBIL load) is a load that creates no inflection points and positive bending moments is a selected inspection region of the beam [12]. For a simply supported beam, for example, a PBIL load that can be applied is a set of unitary forces applied to each measured DOF (Fig. 3b)—i.e., the same type of load vector considered in the PSIL method.

The theory and the assumptions behind the PSIL method and the PBIL method represents the backbone of the damage detection procedure that was used in this paper to test the effectiveness of the PFR matrix. Such a procedure is composed by the following steps, also shown in the flowchart of Fig. 4.

4.1 Step 0

The data acquisition should be performed to have a training dataset (which is related to the baseline structure) and testing datasets (which are related to the possibly damaged states). According to the used procedure, the vibration output of the baseline structure state must be recorded for a period equal to LT, so that it can be segmented in number of L segments of length T. As shown in the following steps this is required to set a threshold for the used damage index, and it is evident that the higher the number L, the more accurate will be the estimation of the statistical variability of the damage-sensitive features related to the baseline structure. Referring to the testing dataset, the length of the measurements should be at least equal to T for each possibly damaged state.

4.2 Step 1

The proportional flexibility-resembling matrices $\boldsymbol{F}_{\boldsymbol{B}}^{*}$ and $\boldsymbol{F}_{\boldsymbol{I}}^{*}$ are estimated for the baseline and the inspection states, respectively. It is important to underline that, to make a proper comparison between the different structural states, the PFR matrices for the baseline and the inspection states should be estimated by considering the same sampling

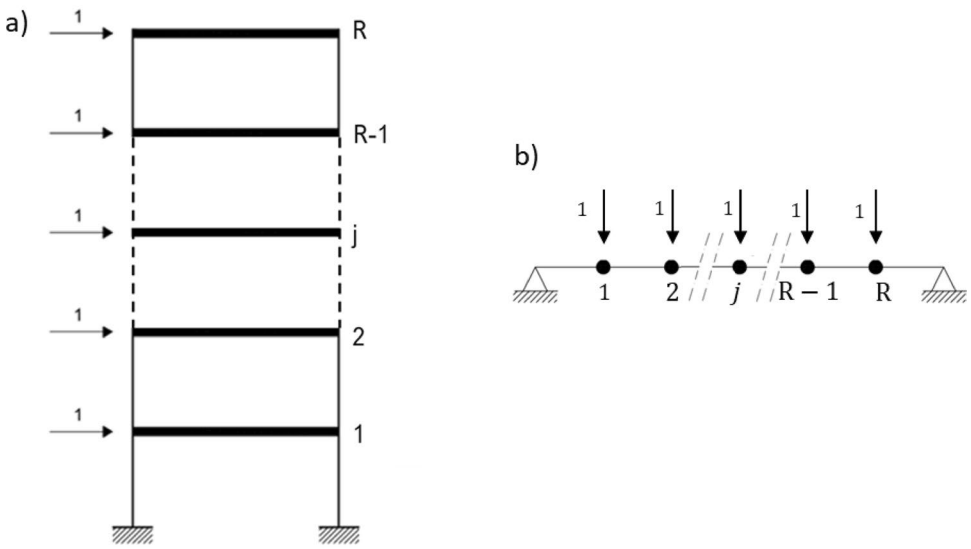

Fig. 3 Structural models with applied inspection loads: **a** shear building structure with a set of unitary forces applied to each story (i.e., a positive shear inspection load); **b** beam-like structure with a set of unitary forces applied to each measured DOF (i.e., a positive bending inspection load)

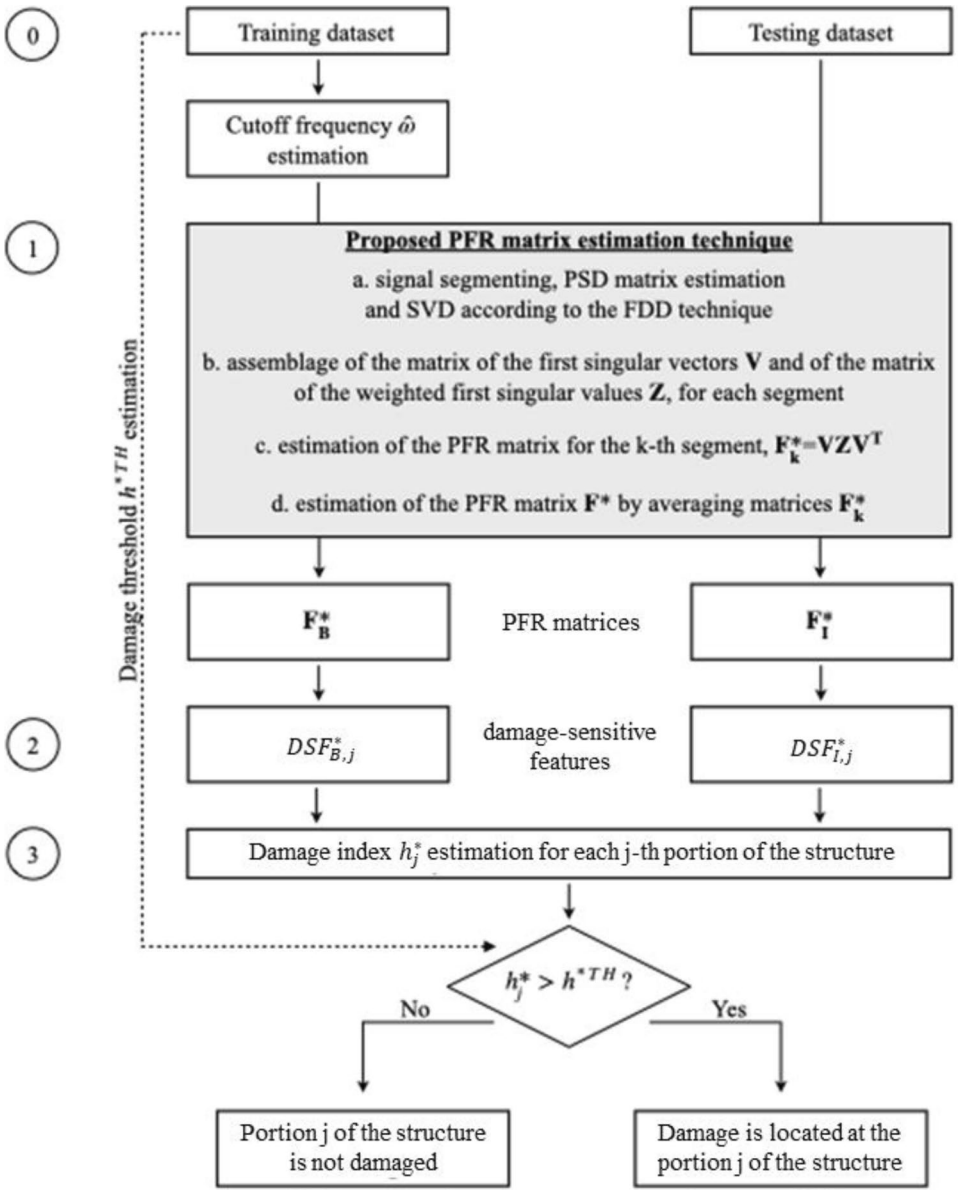

Fig. 4 Damage detection method based on the proposed PFR matrix

frequency, the same frequency resolution, and the same cutoff frequency. Each PFR matrix can be estimated using the steps described in Sect. 3, which can be summarized as follows:

(a) Each k-th segment of the response signal (with length T_8) is processed to estimate its power spectral density matrix $\boldsymbol{G_y}(n\Delta\omega)$. A singular value decomposition of the PSD matrix is performed, according to the frequency domain decomposition technique—i.e., $\boldsymbol{G_y}(n\Delta\omega) = \boldsymbol{U}_n\boldsymbol{S}_n\boldsymbol{U}_n^H$.

(b) For all the sampled frequencies, the first singular vector of $\boldsymbol{G_y}(n\Delta\omega)$, namely the first column of $\boldsymbol{U}_n$, is converted into the real vector $\boldsymbol{v_n}$. Then, all the resulting vectors are assembled into the matrix of the first singular vectors $\boldsymbol{V}$—i.e.,$\boldsymbol{V} = \left[\boldsymbol{v}_1, \boldsymbol{v}_2, \ldots, \boldsymbol{v}_{N/2}\right]$. At the same time, the first singular values s_n are used to form the diagonal matrix $\boldsymbol{Z} = diag\left(\frac{s_n\varepsilon_n}{\omega_n^c}\right)$. This matrix thus contains the weighted first singular values, and through the discrimination function ε_n (Eq. 12) all the terms that correspond to frequencies below the cutoff frequency $\hat{\omega}$ are set to be 0. In the matrix $\boldsymbol{Z}$ the frequency exponent c is dependent on the type of the recorded signal ($c = -1$ for displacement, $c = 1$ for velocity, $c = 3$ for acceleration). It is expected that the proposed PFR matrix could be estimated and used starting from other types of measurements, such as dynamic strain measurements. This, however, requires dedicated analyses, and it will be tested in future research.

(c) The proportional flexibility-resembling matrix is calculated for the considered k-th segment of the response signal as $\boldsymbol{F}_{\boldsymbol{k}}^{*} = \boldsymbol{V}\boldsymbol{Z}\boldsymbol{V}^{T}$.
(d) The PFR matrix $\boldsymbol{F}^{*}$ for the considered state (e.g., baseline or inspected state) is given by the average of all the resulting $\boldsymbol{F}_{\boldsymbol{k}}^{*}$ matrices.

4.3 Step 2

Considering that $\boldsymbol{F}^{*}$ resembles a proportional flexibility matrix, virtual inspection loads can be applied to the estimated flexibility-based model to calculate the deflections $\boldsymbol{\delta}^{*}$. Specifically, after having estimated the proportional flexibility-resembling matrices $\boldsymbol{F}_{\boldsymbol{B}}^{*}$ and $\boldsymbol{F}_{\boldsymbol{I}}^{*}$, which are related to the baseline state and to the inspection state, respectively, the corresponding deflections $\boldsymbol{\delta}_{\boldsymbol{B}}^{*}$ and $\boldsymbol{\delta}_{\boldsymbol{I}}^{*}$ are calculated by applying the load $\boldsymbol{b}$ for each considered state:

$$\boldsymbol{\delta}^{*} = \boldsymbol{F}^{*}\boldsymbol{b} \tag{16}$$

When considering shear building structurers, according to the PSIL method, the interstory drifts are estimated from the deflections and considered as damage-sensitive features. The j-th component of the interstory drift vector $\boldsymbol{d}^{*}$ can be calculated as follows:

$$d_{j}^{*} = \begin{cases} \delta_{j}^{*} - \delta_{j-1}^{*}, & \text{for} \quad j = 2 \ldots R \\ \delta_{j}^{*}, & \text{for} \quad j = 1 \end{cases} \tag{17}$$

where δ_{j}^{*} is the j-th component of the deflection vector $\boldsymbol{\delta}^{*}$. The drift vectors related to the baseline and inspection state are indicated as $\boldsymbol{d}_{\boldsymbol{B}}^{*}$ and $\boldsymbol{d}_{\boldsymbol{I}}^{*}$, respectively. When considering beam-like structures, according to the PBIL method, the curvature of the deflections can be estimated using the finite difference approach for the numerical derivation and considered as damage-sensitive feature. The curvature at a generic DOF can be determined as follows:

$$\chi_{j}^{*} = \frac{\delta_{j+1}^{*} - 2\delta_{j}^{*} + \delta_{j-1}^{*}}{\Delta l^{2}} \tag{18}$$

The approach of Eq. (18) can be applied when the measured DOFs are positioned at a constant spacing Δl, and this layout with a constant spacing is the most common layout of instrument locations typically used in practice. Equation (18) can be directly derived from the approach for curvature estimation valid in the more general case of instrument locations that are unevenly distributed, shown in [11]. The curvature vectors related to the baseline and inspection state are indicated as $\boldsymbol{\chi}_{\boldsymbol{B}}^{*}$ and $\boldsymbol{\chi}_{\boldsymbol{I}}^{*}$, respectively.

4.4 Step 3

This final step is related to the evaluation of the damage index and to the execution of statistical tests for damage localization. To this purpose, it is important to underline that, since $\boldsymbol{F}^{*}$ is directly estimated from the measured response through signal processing operations, the scaling factors (present between estimated PFR matrices and true modal flexibility matrices) could be dependent on the amplitude of the ambient excitation. Such an amplitude could vary between two different measurements (for example related to the baseline and inspection state), and as a result this may lead to damage-sensitive features (i.e., interstory drift vectors or curvature vectors) with different scaling factors. A similar problem has already been addressed in [16, 17], to deal with proportional flexibility matrices and drift vectors of shear building structures that are characterized by different and unknown scaling factors. Specifically, in [16, 17] it is shown that such quantities cannot be compared using traditional metrics, such as the metrics based on the difference between the DSFs in the inspection and baseline state used in the original formulation of the PSIL method. Instead, a specific damage index, termed h^{*} index, has been introduced in [16, 17] for performing the damage localization using DSFs with different scaling factors. This index presented in [16, 17] is thus also employed in the damage detection procedure applied in this paper using the proportional flexibility-resembling matrix $\boldsymbol{F}^{*}$. When considering shear building structures, the h_{j}^{*} index has to be evaluated for each j-th story using the interstory drifts (Eq. 17) as DSFs. When considering flexure-type beam-like structures, the h_{j}^{*} index has to be evaluated for each j-th measured DOF using the values of the curvature (Eq. 18) as DSFs. The h_{j}^{*} index is defined as follows:

$$h_{j}^{*} = \frac{DSF_{I,j}^{*}/DSF_{B,j}^{*}}{\min\limits_{j=1\ldots R}\left(DSF_{I,j}^{*}/DSF_{B,j}^{*}\right)} - 1 \tag{19}$$

The j-th portion of the structure is undamaged if $h_{j}^{*} = 0$, where this generic portion corresponds to a generic story for shear building structures and to a generic measured DOF for flexure-type beam-like structures. Otherwise, damage is localized at the j-th portion of the structure if $h_{j}^{*} > 0$. To deal with the uncertainties that affect the damage-sensitive features, it is necessary to define a threshold h^{*TH} so that damage is localized at the portions of the structure for which $h_{j}^{*} > h^{*TH}$. The threshold is empirically calculated from the training data set, through the following steps. At first, the h^{*} index is evaluated by comparing the DSFs estimated from the first segment of the training dataset with the DSFs obtained for each of the other $L-1$ data segments, by

applying the following expression for each j-th portion of the structure:

$$h_{ij}^{*} = \frac{DSF_{i,j}^{*}/DSF_{1,j}^{*}}{\min\limits_{j=1\ldots R}\left(DSF_{i,j}^{*}/DSF_{1,j}^{*}\right)} - 1 \tag{20}$$

where $DSF_{1,j}^{*}$ is the damage-sensitive feature obtained from the first data segment (i.e., $i = 1$) and $DSF_{i,j}^{*}$ is the damage-sensitive feature calculated for the i-th segment with $i = 2 \ldots L$. Then, starting from the values obtained using Eq. (20), the threshold h^{*TH} is estimated as follows:

$$h^{*TH} = \max_{i=2\ldots L}\left(\max_{j=1\ldots R} h_{ij}^{*}\right) \tag{21}$$

It is worth noting that, as stated in [16], the h_j^{*} index is suitable for detecting localized damage (either single or multiple damage), while the index is theoretically not sensitive to a uniformly distributed damage pattern (e.g., a uniform stiffness reduction in all the stories of the shear building). According to the formulation shown in [16], this last damage scenario (which is not common in practice) can be addressed by performing more advanced scaling operations on the proportional flexibility matrices or using more traditional approaches not based on proportional unscaled damage-sensitive features.

5 Basic principles behind the PFR matrix estimation

Let us consider, for simplicity, the displacement signal-based formula of $\boldsymbol{F}^{*}$, as it is shown in Eq. (8), so that the results are not affected by the choice of the cutoff frequency $\widehat{\omega}$. This way, the generic element of $\boldsymbol{F}^{*}$ can be written as:

$$f_{jk}^{*} = \sum_{n=1}^{N/2} v_{jn} v_{kn} z_n \tag{22}$$

In general, if the structure is lightly damped and with well separated modes, the spectrum of the response can be divided in bands where a single mode only is dominating, with no gaps between two consecutive bands. Such division can be done by following the theory behind the FDD technique [1]. Given the natural frequency $\omega_r = n_r \Delta\omega$ of the r-th mode, $s_d\left(n_r \Delta\omega\right)$ will be a relative maximum point and the first singular vector $\boldsymbol{u}_{1\boldsymbol{r}}$ of $\boldsymbol{G}_{\boldsymbol{y}}\left(n_r \Delta\omega\right)$ can be considered as a good estimation of the corresponding mode shape $\boldsymbol{\psi}_{\boldsymbol{r}}$. When moving away from the peak, the influence of the eigenvalues of the other modes start to interfere, but, as long as only the first singular value s_{dn} is significantly different from zero, the correlation between the first singular vectors of the PSD matrix and $\boldsymbol{u}_{1\boldsymbol{r}}$ is high, and s_{dn} can be considered as the auto spectral density function $g_r^2(n\Delta\omega)$ of the r-th modal coordinate. Thus, it is possible to consider the boundaries of the band dominated by mode r as the frequencies for which s_{dn} presents the first local minimum points, before and after ω_r. In other words, it is possible to state that the r-th mode band is limited to the left by the boundary frequency $\omega_{r-1,r} = n_{r-1,r}\Delta\omega$ and to the right by frequency $\omega_{r,r+1} = n_{r,r+1}\Delta\omega$, so that $s_d\left(\omega_{r-1,r}\right)$ and $s_d\left(\omega_{r,r+1}\right)$ are two consecutive minimum points of the discrete function $s_d(n\Delta\omega)$; the division of the spectrum applied in Fig. 5 can be taken as an example. Considering this, and highlighting that singular vectors (and consequently all vectors $\boldsymbol{v}_{\boldsymbol{n}}$) are unit scaled, Eq. (22) implies that:

- inside the r-th mode frequency band, the closer the frequency ω_n is to ω_r, the higher is the correlation between the corresponding vector $\boldsymbol{v}_{\boldsymbol{n}}$ and $\boldsymbol{\psi}_{\boldsymbol{r}}$;

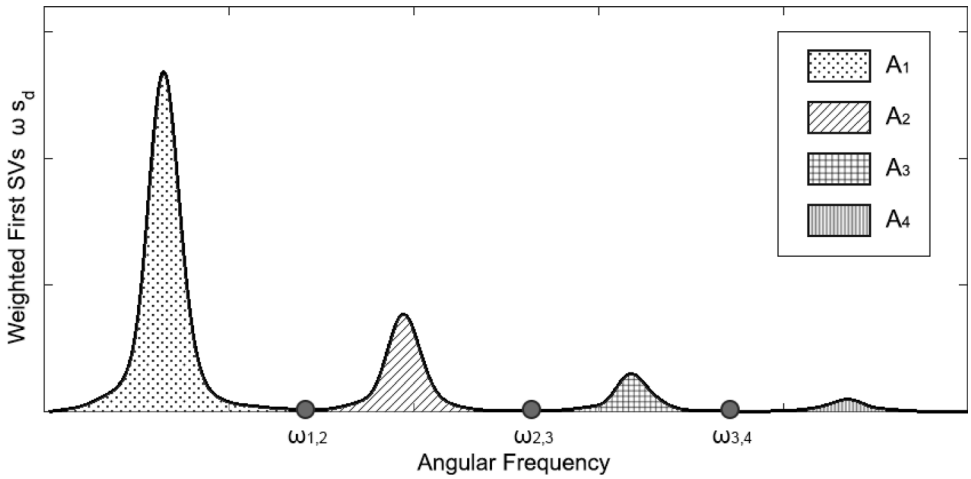

Fig. 5 Exemplification of a plot of weighted first singular values ωs_d where the areas underneath the function for frequencies between $\omega_{r,r-i}$ and $\omega_{r,r+i}$ are highlighted

- inside the r-th mode frequency band, the closer the frequency ω_n is to ω_r, the higher is the corresponding first singular value s_{dn}.

These two statements are the basis of the theoretical approach related to the formulation of the proportional flexibility-resembling matrix $\boldsymbol{F}^*$: first singular vectors with high correlation to mode shapes have higher contribution to $\boldsymbol{F}^*$, being multiplied by a higher first singular value; on the contrary, first singular vectors with low correlation are almost neglected, being multiplied by vanishing singular values.

As shown in Appendix A, it is possible to state that for a structure with perfectly regular distribution of masses the contribution ratio between generic modes r and s to the flexibility matrix is given by:

$$\xi_{rs} = \frac{\omega_s^2}{\omega_r^2} \tag{23}$$

A similar index can be defined for the PFR matrix $\boldsymbol{F}^*$, considering the aforementioned division of the spectrum of the response. While in the MF matrix the contribution of the r-th mode is proportional to the term $1/\omega_r^2$, in the proposed PFR matrix the different contributions are associated to the different mode frequency bands, and for a generic r-th band the contribution is proportional to the sum of all the weighted first singular values that are inside the band itself. It follows that the contribution ratio ρ_{rs} between modes r and s to the proportional flexibility-resembling matrix $\boldsymbol{F}^*$ is given by:

$$\rho_{rs} = \frac{\sum_{n=n_{r-1,r}}^{n_{r,r+1}} z_n}{\sum_{n=n_{s-1,s}}^{n_{s,s+1}} z_n} \tag{24}$$

By multiplying both the numerator and the denominator of Eq. (24) by the frequency resolution $\Delta\omega$, and considering the continuous spectrum (i.e., $\Delta\omega \to 0$), Eq. (24) expresses the ratio between the areas A_r and A_s underneath the curve of the continuous function $z(\omega) = \omega s_d(\omega)$, in frequency bands where modes r and s are respectively dominating, as it is shown in Fig. 5. This way, the ρ_{rs} ratio can be expressed as:

$$\rho_{rs} = \frac{\int_{\omega_{r-1,r}}^{\omega_{r,r+1}} z(\omega)d\omega}{\int_{\omega_{s-1,s}}^{\omega_{s,s+1}} z(\omega)d\omega} = \frac{A_r}{A_s} \tag{25}$$

The ρ_{rs} index is directly derived from Eq. (8) of $\boldsymbol{F}^*$ and from Eq. (22). Specifically, all the weighted singular values describing the r-th modal bell in the spectrum are cumulated to determine the contribution of the r-th mode in the PFR matrix.

6 PFR matrix: derivation and calibration of the procedure

The expressions of the PFR matrix which were introduced beforehand have been derived through a parametric analysis, aimed at calibrating the procedure used to weigh the first singular values through the corresponding angular frequencies (i.e., matrices $\boldsymbol{Z}$ and $\boldsymbol{Z_d}$ of Eqs. (11) and (7), respectively). Specifically, the parametric analysis was performed to find out which value of the exponent of ω can maximize the level of resemblance between the PFR matrix and the modal flexibility matrix, and thus the problem was addressed as an optimization problem.

Since singular values of acceleration, velocity and displacement PSD matrices are related as shown in Eq. (10), there is no need to analyze the spectra of all these different quantities. The analyses were performed by considering acceleration signals, and at the end the findings of this study were extended to the case of the displacement and velocity signals by considering the time-differentiation rules in the frequency domain.

The first step in the process was made by introducing a generalized expression of the modal contribution ratio $\rho_{rs}(\gamma)$, where the first singular values $s_a(\omega)$ of the PSD matrix of an acceleration signal are considered. The $\rho_{rs}(\gamma)$ indexes are function of the exponent γ of the angular frequency, and the exponent γ is the main parameter that characterizes the parametric study presented in this section. Moreover, the $\rho_{rs}(\gamma)$ indexes are calculated as the average results over a number ϑ of segments of the signal (so that, for the k-th segment, $s_{ak}(\omega)$ is the first singular value):

$$\rho_{rs}(\gamma) = \frac{1}{\vartheta}\sum_{k=1}^{\vartheta}\left[\frac{\int_{\omega_{r-1,r}}^{\omega_{r,r+1}}\left(s_{ak}(\omega)/\omega^{\gamma}\right)d\omega}{\int_{\omega_{s-1,s}}^{\omega_{s,s+1}}\left(s_{ak}(\omega)/\omega^{\gamma}\right)d\omega}\right] \tag{26}$$

Similarly to Eq. (25), $\rho_{rs}(\gamma)$ is the averaged ratio between the areas underneath the curves of the functions $s_{ak}(\omega)/\omega^{\gamma}$, inside of frequency bands where modes r and s are, respectively, dominating.

Three different structures were considered in the numerical simulation:

1. A 10-story shear-type building, modeled using 10 DOFs, equal floor masses $m = 22.50 \times 10^3$kg and interstory stiffness of each story equal to $k_j = 4.23 \times 10^5$kN/m;
2. A simply supported beam, modeled using 10 DOFs (so that 10 discrete masses m are placed with a regular distance interval of 5 m, replacing the continuous distribution of the mass in this model), rectangular transversal section (3 m in height, 0.2 m in width), Young modulus $E = 33.02 \times 10^6$kN/m^2;

3. A cantilever beam, modeled using 10 DOFs, so that masses m are placed with a regular distance interval of 3 m, rectangular transversal section (3 m in height, 0.3 m in width), and the same Young modulus of the previous structure.

All the considered structures are classically damped, so that the modal damping ratio $\nu = 5\%$ is constant for each mode. All the models were excited by white noise inputs at all the DOFs, simulating the ideal type of excitation present in structures subjected to ambient vibrations, and the output dynamic response was recorded using a sample frequency $f_s = 128$Hz, with a total duration of 1920s. Once the structural responses were collected, the signal was divided in $\vartheta = 30$ segments. For all three planar models, the direction of the applied inputs and of the recorded responses is the transverse direction.

In Fig. 6, the response of the shear-type building is considered to plot the functions $s_a(\omega)/\omega^\gamma$ for integer values of γ between 0 and 4. These functions were divided by their respective maximum value to ease the comparison. It is possible to observe that only for $\gamma = 0$ (i.e., considering the first singular values of the acceleration PSD matrix), there is not a descending trend in the amplitude of the peaks of the curve. For all the other values of γ, instead, the amplitude of the peaks decreases when frequency increases; furthermore, it is clearly shown that the higher is the value of γ, the lower are the peaks of the high-order modes in comparison to the peaks of the low-order modes. For instance, in case of $\gamma = 4$ (i.e., the displacement power spectrum of the signal is considered) only the first two modes can be distinguished, while the third and the fourth peaks cannot be perceived in linear scale.

The modal contribution ratios $\rho_{12}(\gamma)$ and $\rho_{13}(\gamma)$ have been evaluated for the three structures and for the aforementioned values of γ, and the results are reported in Tables 1 and 2. It is clearly shown that the considered modal contribution ratios increase when γ is increased: the trend is confirmed for both $\rho_{12}(\gamma)$ and $\rho_{13}(\gamma)$. This fact can be explained as follows: considering that each modal bell is multiplied by the term $1/\omega^\gamma$,

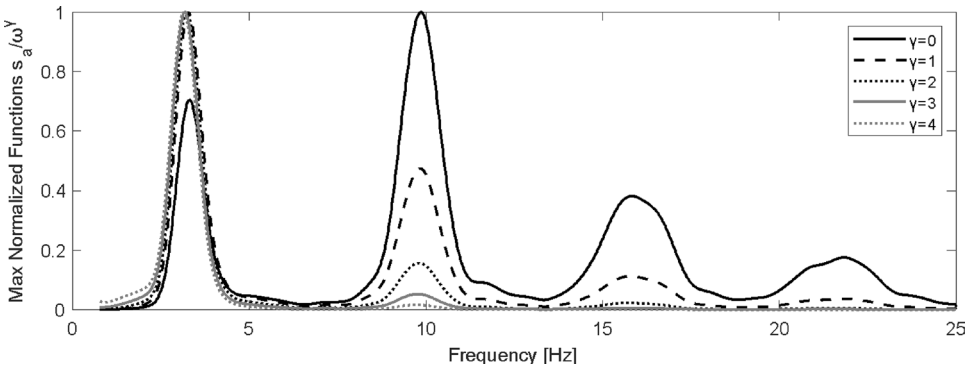

Fig. 6 Functions of weighted first singular values $s_a(\omega)/\omega^\gamma$ evaluated for different values of γ (10-story shear building model; functions normalized to the maximum value)

Table 1 Comparison between the modal contribution ratios in the MF matrix ξ_{12} and the modal contribution ratios in the PFR matrix $\rho_{12}(\gamma)$ evaluated for different values of γ (structures modeled using 10 DOFs; first and second modes are considered)

Structure	$\xi_{12} = \frac{\omega_2^2}{\omega_1^2}$	Ratio of areas underneath modal bells, $\rho_{12}(\gamma)$				
		$\gamma = 0$	$\gamma = 1$	$\gamma = 2$	$\gamma = 3$	$\gamma = 4$
Shear-type building	8.9	0.4	1.0	3.6	8.9	26.9
Simply supported beam	16.1	0.3	1.1	4.6	16.7	71.3
Cantilever beam	40.1	0.2	1.2	6.7	42.6	278.5

Table 2 Comparison between the modal contribution ratios in the MF matrix ξ_{13} and the modal contribution ratios in the PFR matrix $\rho_{13}(\gamma)$ evaluated for different values of γ (structures modeled using 10 DOFs; first and third modes are considered)

Structure	$\xi_{13} = \frac{\omega_3^2}{\omega_1^2}$	Ratio of areas underneath modal bells, $\rho_{13}(\gamma)$				
		$\gamma = 0$	$\gamma = 1$	$\gamma = 2$	$\gamma = 3$	$\gamma = 4$
Shear-type building	23.9	0.3	1.0	7.4	28.6	134.6
Simply supported beam	81.6	0.2	1.1	14.4	88.0	915.6
Cantilever beam	316.6	0.1	1.2	26.0	349.0	7176.5

the areas underneath the spectral bells of higher modes will reduce as far as γ is increased.

In Tables 1 and 2, the most noticeable fact emerges by comparing the $\rho_{rs}(\gamma)$ indexes related to the PFR matrix with the corresponding ξ_{rs} index related to the MF matrix: considering $\gamma = 3$, the two indexes tend to converge to the same number, so that for the analyzed cases it is possible to state that $\rho_{rs}(3) \cong \xi_{rs}$. This is one of the most important results that were obtained in the process of deriving the proposed PFR matrix. Specifically, it has been obtained that dividing the first singular value of the PSD matrix of the acceleration response by the angular frequency with an integer exponent equal to $\gamma = 3$, the areas underneath the spectral bells (in the function of the weighted first singular values) tend to be directly proportional to the contribution of the corresponding modes in the modal flexibility matrix.

In the previous analysis, the considered modal damping ratios are constant for all the modes. To evaluate if damping variations have an influence on the obtained results, a correlation analysis between different values of the modal damping and the modal contribution ratios was performed. A proportional damping model was considered [34], so that the modal damping matrix can be expressed as:

$$\boldsymbol{\Xi} = \mathrm{diag}\left(2\nu_r\omega_r\right), r = 1 \ldots R \tag{27}$$

where ν_r is the modal damping ratio related to the r-th mode. The numerical simulation of the dynamic response of the previously described shear-type building was considered, and the resulting value $\gamma = 3$ from the previous analysis was maintained. In the analysis, 50 different values of the first modal damping ratio ν_1 were introduced to vary the quantity ν_2/ν_1. For each value of ν_2/ν_1, the modal contribution ratio $\rho_{12}(3)$ was estimated as the average over a number $\vartheta = 5$ of segments, and the results are gathered in Fig. 7. The results show a noticeably high level of correlation between the two variables, and the resulting 50 points of the plot are almost perfectly aligned. This fact, together with the results of Tables 1 and 2, have led to the following deductions:

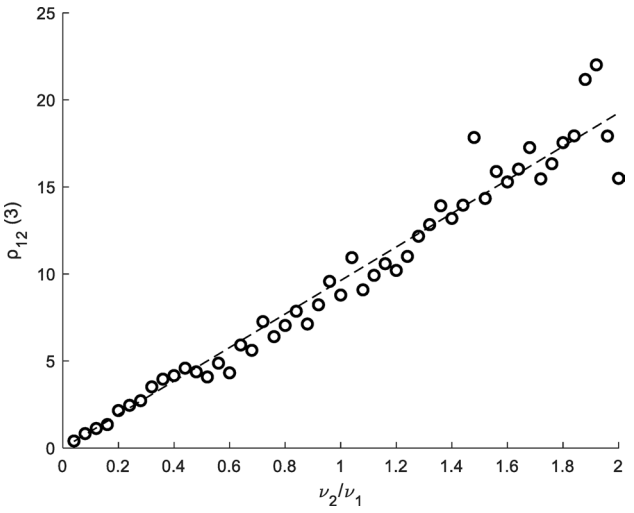

Fig. 7 Correlation analysis between the modal contribution ratios $\rho_{12}(3)$ and the modal damping ratios

- The modal contribution ratios ρ_{rs} given by Eq. (25) can be considered equal to the respective ξ_{rs} from Eq. (23) as far as $\nu_s/\nu_r = 1$;
- The ratios ρ_{rs} and ν_s/ν_r can be assumed as directly proportional;
- From the statement above, it is evident that the modal contribution of the r-th mode to $\boldsymbol{F}^*$ is inversely proportional to its corresponding damping ratio.

Consequently, from the performed correlation analysis it is recognized that the influence of damping to the level of resemblance between $\boldsymbol{F_p}$ and $\boldsymbol{F}^*$ has to be studied. Specifically, the calibration of the procedure used to weigh the first singular values in the PFR matrix estimation was performed by considering structures with different damping models.

Let us now introduce $\boldsymbol{F}^*(\gamma)$, which is the expression of the PFR matrix in function of the γ exponent that was used in the following analyses:

$$\boldsymbol{F}^*(\gamma) = \boldsymbol{V}\boldsymbol{Z}(\gamma)\boldsymbol{V}^T \tag{28}$$

where the matrix of the weighted singular values $\boldsymbol{Z}(\gamma)$ is now expressed specifically in function of the acceleration first singular values s_{an} and the parameter γ:

$$\boldsymbol{Z}(\gamma) = \mathrm{diag}\left(\frac{s_{an}\epsilon_n}{\omega_n^\gamma}\right), \quad n = 1 \ldots \frac{\mathrm{N}}{2} \tag{29}$$

Of course, the considered $\boldsymbol{F}^*(\gamma)$ matrix is obtained by averaging the results of the ϑ segments, as shown in Sect. 3, and the generic term of such a matrix is $f_{jk}^*(\gamma)$.

To analyze the effects of damping, and consequently to define the value of γ that maximizes the level of resemblance between $\boldsymbol{F}^*(\gamma)$ and $\boldsymbol{F_p}$, five damping models were used. The first implemented damping model is the one that was already considered in the first analysis—i.e., a proportional damping model with all the modal damping ratios that are equal to 5%. The other four cases rely on Rayleigh-damping models [37]: thus, the assumption is that the damping matrix $\boldsymbol{C}$ can be assumed as a linear combination of the mass matrix $\boldsymbol{M}$ and the stiffness matrix $\boldsymbol{K}$:

$$\boldsymbol{C} = \alpha\boldsymbol{M} + \beta\boldsymbol{K} \tag{30}$$

In Eq. (30), $\boldsymbol{C}$, $\boldsymbol{M}$ and $\boldsymbol{K}$ are $R \times R$ matrices, while α and β are scalar combination coefficients.

While matrices $\boldsymbol{M}$ and $\boldsymbol{K}$ do not vary in the performed simulation, the definition process and properties of matrix $\boldsymbol{C}$ are described for each case, as follows:

- Case 1: Modal damping ratio $\nu = 5\%$ is equal for each mode. This way, the damping matrix is given by $\boldsymbol{C} = \boldsymbol{\Phi}^{-T}\boldsymbol{\Xi}\boldsymbol{\Phi}^{-1}$;
- Case 2: An only mass-proportional damping is considered and formulated with Eq. (30) by assuming $\alpha = 2$ and $\beta = 0$;
- Case 3: An only stiffness-proportional damping is considered and formulated with Eq. (30) by assuming $\alpha = 0$ and $\beta = 0.002$;
- Case 4: The complete form of Rayleigh damping is taken, assuming $\alpha = 1$ and $\beta = 0.001$;
- Case 5: The complete form of Rayleigh damping is taken, similarly to Case 4, but in this case $\alpha = 2$ and $\beta = 0.0005$.

Combining Eqs. (27) and (30), the general formula of the modal damping ratio of a generic mode r is the following:

$$\nu_r = \frac{1}{2}\left(\frac{\alpha}{\omega_r} + \beta\omega_r\right) \tag{31}$$

where the damping ratio is expressed as a function of the natural angular frequency and the scalar combination coefficients α and β of the Rayleigh-damping model. From Eq. (31), it is clear that the modal damping ratios decrease as the mode order increases in the case of only mass-proportional damping, while the opposite happens for only stiffness-proportional damping models. In other words, it is possible to state that only mass- and only stiffness-proportional damping models can be assumed as extreme theoretical cases, while models in which both α and β differ from 0 do not present a unique trend of the modal damping in function of the mode order. Given this, the four Rayleigh-damped cases were modeled by setting the coefficients α and β in a way that they are associated to realistic values of the damping ratios of the first three modes (i.e., around 5%), so that the structure can be considered as lightly damped.

Two different approaches were implemented to evaluate the best fitting value of γ, considering the simulated dynamic response of the aforementioned shear-type structure.

The first approach follows directly what has already been presented and is based on a comparison in terms of modal contribution ratios. Specifically, the index $\eta_{rs}(\gamma)$ was introduced in the analyses to measure the difference between the modal contribution ratios related to the PFR and the MF matrices ($\rho_{rs}(\gamma)$ and ξ_{rs}, respectively):

$$\eta_{rs}(\gamma) = \frac{\left|\rho_{rs}(\gamma) - \xi_{rs}\right|}{\max\left(\left|\rho_{rs}(\gamma) - \xi_{rs}\right|\right)} \tag{32}$$

The $\eta_{rs}(\gamma)$ index was separately evaluated for all five cases with different damping models that are mentioned above, considering values of γ between 0 and 5. The index tends to 0 for values of γ that make $\rho_{rs}(\gamma)$ equal to ξ_{rs}, while it assumes its maximum of 1 for the value of γ that maximizes the discrepancy between $\rho_{rs}(\gamma)$ and ξ_{rs}. The results for all five cases are shown in Fig. 8a–e, by considering the values of the index $\eta_{12}(\gamma)$ – i.e., the first two modes are considered. For all these cases, the minimum of $\eta_{12}(\gamma)$ is found for the considered range of γ and always assumes values that are close to 0. This implies that for these minimum values, the contribution ratios $\rho_{rs}(\gamma)$ and ξ_{rs} of the first two modes are very similar.

Figure 8a confirms 3 is the best fitting value of γ in case of constant modal damping ratios; on the contrary, Fig. 8b and c show the limit values of γ for a Rayleigh-damping modeled structure. Specifically, these figures illustrate that $\eta_{12}(4)$ and $\eta_{12}(2)$ are, respectively, the minimum values in case of only mass- and only stiffness-proportional damping, pointing out that the best fitting value of γ in case of proportional damping can assume values between 2 and 4. Other analyses were performed by changing the values of α and β, as well as by changing the value of the constant modal damping ratio, and the obtained results are similar to the ones that have just been presented. Figure 8d and e clearly shows that for the chosen cases of both mass and stiffness proportional damping, the minimum values of $\eta_{12}(\gamma)$ occur for values of γ that are close to 3 (i.e., $\gamma = 3$ and $\gamma = 3.4$ for case 4 and 5, respectively). It is also worth noting that, for all the considered cases, the value $\eta_{12}(3)$ is far below 0.1, with the only exception of Case 2, where the value $\eta_{12}(3)$ is slightly lower than 0.3.

The last step of this analysis implied the evaluation of the summation plot $\sum \eta_{12}(\gamma)$, where the values of $\eta_{12}(\gamma)$ of the five cases are summed. The bar graph is shown in Fig. 8f. As it is evident in the plot, the value $\gamma = 3$ is the one that minimizes the summation of $\eta_{12}(\gamma)$ for all the considered cases, thus giving the lowest discrepancies between the modal contribution ratios of the MF and the PFR matrices. It is worth noting that $\gamma = 3$ is also the middle point value between the mentioned limit values $\gamma = 2$ and $\gamma = 4$.

In the second approach adopted to find the best fitting value of γ, the level of resemblance between $\boldsymbol{F}^*(\gamma)$ and the MF matrix $\boldsymbol{F_p}$ was globally evaluated, and this was done using a specific matrix norm operator, as described in the following. In this analysis, all modes are considered in $\boldsymbol{F_p}$ (i.e., $p = 10$), to exclude the effects of the modal truncation in the results; in the same way, the sampling

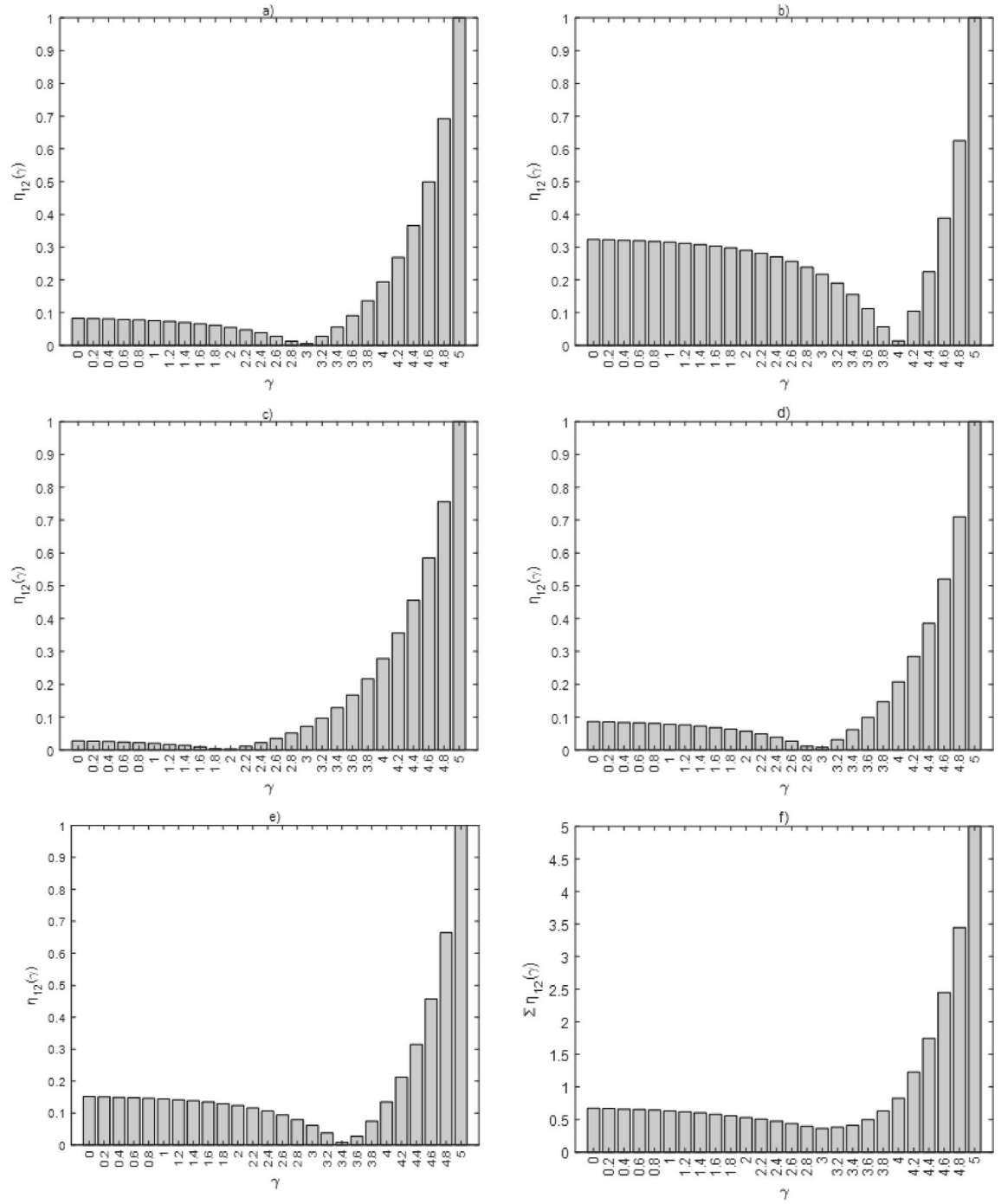

Fig. 8 Difference between the modal contribution ratio in the PFR matrix and the modal contribution ratio in the MF matrix; parametric study with the quantity η_{12} expressed as a function of γ; results for five different models of damping: **a** case 1; **b** case 2; **c** case 3; **d** case 4; **e** case 5; **f** total summation for the different cases

frequency was chosen so that all mode spectral bells can contribute to the assemblage of $\boldsymbol{F}^*(\gamma)$.

In the performed analysis, the element-wise 1-norm operator was used, which for a generic $R \times R$ matrix $\boldsymbol{A}$ is defined as $\|\boldsymbol{A}\|_{1,1} = \sum_{j=1}^{R} \sum_{k=1}^{R} \left|a_{jk}\right|$. This matrix norm operator was used to evaluate the unit-normalized MF matrix $\overline{\boldsymbol{F}}_{\boldsymbol{p}} = \frac{1}{\|\boldsymbol{F}_{\boldsymbol{p}}\|_{1,1}} \boldsymbol{F}_{\boldsymbol{p}}$ (whose generic element is

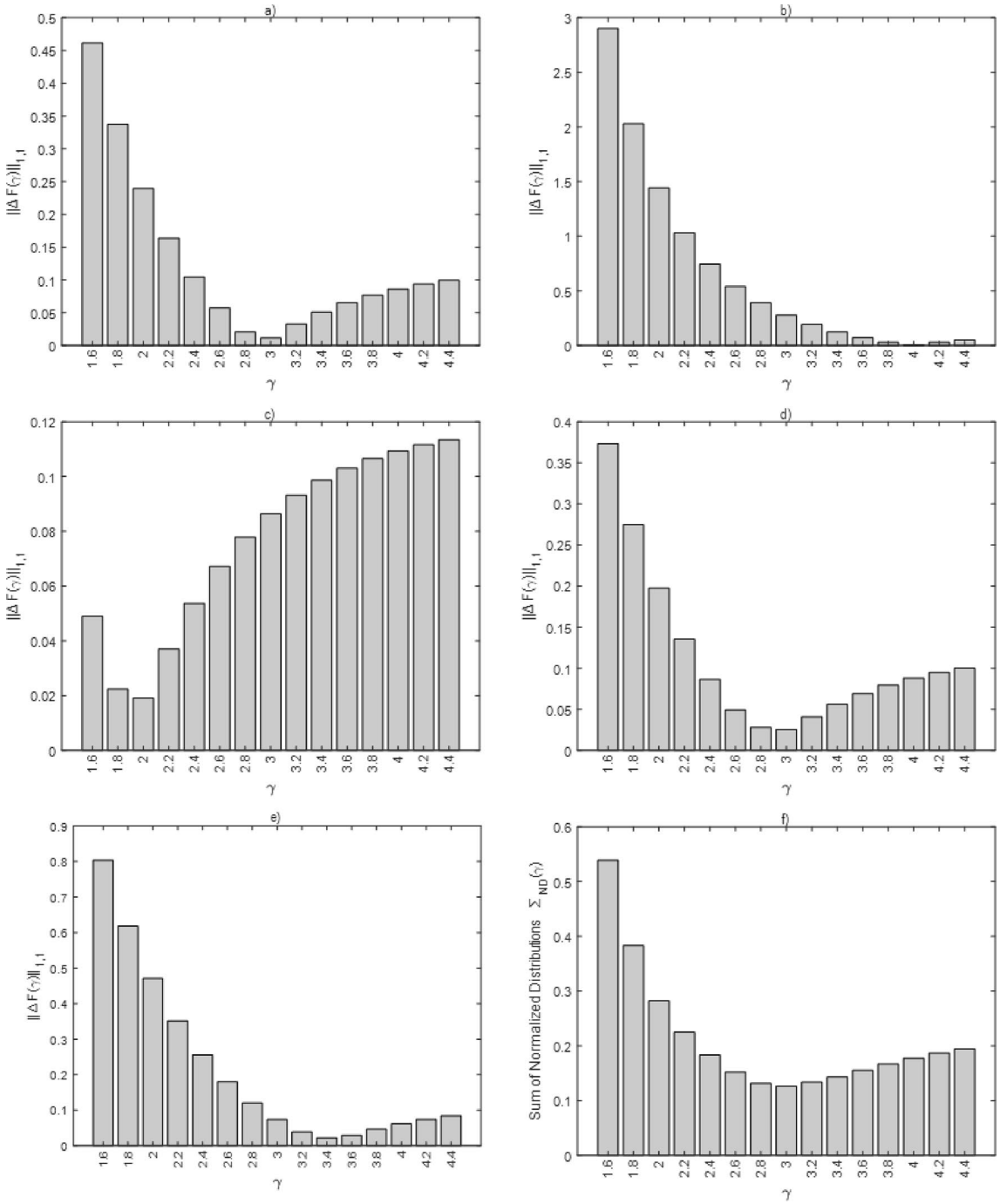

Fig. 9 Norm of the difference between the PFR matrix and the MF matrix; parametric study as a function of γ; results for five different models of damping: **a** case 1; **b** case 2; **c** case 3; **d** case 4; **e** case 5; **f** sum of the normalized distributions

$\overline{f}_{p,jk} = \frac{1}{\|\boldsymbol{F_p}\|_{1,1}} f_{p,jk}$) and the unit-normalized PFR matrix in function of the parameter γ, $\overline{\boldsymbol{F}}^*(\gamma) = \frac{1}{\|\boldsymbol{F}^*(\gamma)\|_{1,1}} \boldsymbol{F}^*(\gamma)$ (whose generic element is $\overline{f}^*_{jk}(\gamma) = \frac{1}{\|\boldsymbol{F}^*(\gamma)\|_{1,1}} f^*_{jk}(\gamma)$). Since these two matrices have a common norm, the difference matrix $\Delta \boldsymbol{F}$ was computed and used to evaluate the level of resemblance between $\boldsymbol{F_p}$ and $\boldsymbol{F}^*(\gamma)$:

$$\Delta \boldsymbol{F}(\gamma) = \overline{\boldsymbol{F}}_{\boldsymbol{p}} - \overline{\boldsymbol{F}}^* \tag{33}$$

The norm $\|\Delta \boldsymbol{F}(\gamma)\|_{1,1}$ of the difference matrix was then calculated.

Figure 9a–e shows the variation of $\|\Delta \boldsymbol{F}(\gamma)\|_{1,1}$ obtained for all five cases with different damping models and for values of γ between 1.6 and 4.4 (referring to the values of γ, the plot is focused on the range of interest that has been discussed for the previous results shown in Fig. 8). As it happens by examining the $\eta_{rs}(\gamma)$ indexes, the minimum value of $\|\Delta \boldsymbol{F}(\gamma)\|_{1,1}$ is reached for the value of γ that maximizes the level of resemblance between $\boldsymbol{F}^*(\gamma)$ and $\boldsymbol{F_p}$; on the other hand, the higher is the norm of the difference matrix, the higher are the discrepancies between $\boldsymbol{F}^*(\gamma)$ and $\boldsymbol{F_p}$.

First of all, by comparing Figs. 9 and 8, it is evident that, for all the five cases, the minimum of $\|\Delta \boldsymbol{F}(\gamma)\|_{1,1}$ occurs for the same values of γ that minimize the index $\eta_{12}(\gamma)$ evaluated for the first two modes. This confirms that, as expected, the contribution of these two low-order modes to the MF matrix is higher than the contribution of the high-order modes, and the performed analysis shows that the same occurs in the proposed PFR matrix. Figure 9 also shows that $\|\Delta \boldsymbol{F}(\gamma)\|_{1,1}$ tends to 0 for all the minimum points of the graphs.

Figure 9 illustrates that $\|\Delta \boldsymbol{F}(\gamma)\|_{1,1}$ exponentially decreases when γ increases, until the minimum value is reached; on the other hand, the norm of the difference matrix slowly increases after that point. Specifically, for values of γ on the left of the minimum point, the contribution of the higher modes in the PFR matrix tends to exceed the respective contribution in the MF matrix; the opposite happens to the right of the aforementioned minimum point. From the figure, it is clear that the major discrepancies between the two matrices occur in the former case. It is also relevant to notice that in Fig. 8, for each of the five cases, the distribution of the $\eta_{12}(\gamma)$ values appears mirrored with respect to the distribution of the $\|\Delta \boldsymbol{F}(\gamma)\|_{1,1}$ values. This is due to the fact that $\rho_{12}(\gamma)$ is proportional to the first mode contribution, which is amplified for increasing values of γ (as already shown in Table 1).

The last step of this analysis was performed by evaluating the summation of the aforementioned norms of the difference matrices, for all five cases. A further normalization has been introduced in the distributions shown in Fig. 9a–e, so that all the cases can have the same weight in the summation. Specifically, the mentioned distributions were normalized to their respective maximum value for the considered range of γ, and then the resulting distributions for the different cases were summed. This way, the following quantity was evaluated, and the results are shown in Fig. 9f for the different values of γ:

$$\Sigma_{ND}(\gamma) = \sum_{case\ i=1,2,3,4,5} \left[\frac{\|\Delta \boldsymbol{F}(\gamma)\|_{1,1}}{\max\limits_{\gamma=0\ldots5} \|\Delta \boldsymbol{F}(\gamma)\|_{1,1}} \right]_i \tag{34}$$

As evident in Fig. 9f, the summation of the normalized distributions has a minimum value for $\gamma = 3$, which is again the best fitting value of γ obtained by considering all the different damping models.

Considering the analyses performed in terms of both modal contribution ratios and difference matrices, it is finally possible to state that $\gamma = 3$ is the best value to implement in the definition of $\boldsymbol{F}^*$ because, as shown in the analyses, it tends to minimize the discrepancies between $\boldsymbol{F}^*$ and an actual proportional flexibility matrix, despite of the unknown damping model of the structure. This is the reason that supports the choice of the value of $c = 3$ in Eq. (11) for an acceleration signal, while the other values of c [as well as the terms of matrix $\boldsymbol{Z_d}$ presented in Eq. (7)] were directly derived considering the time-differentiation rules in the frequency domain.

The last step of the parametric study consisted in evaluating the degree of proportionality, between PFR and MF matrices, that is obtained considering the chosen expression of $\boldsymbol{F}^*(\gamma)$ (this means setting $\gamma = 3$). The analysis was conducted for all the five cases with different damping models, by estimating the so-called normalized multipliers between the single elements of $\boldsymbol{F}^*$ and $\boldsymbol{F_p}$:

$$\lambda_{jk} = \frac{R^2 \left(f_{p,jk} / f^*_{jk} \right)}{\sum_{j=1}^{R} \sum_{k=1}^{R} \left(f_{p,jk} / f^*_{jk} \right)} \tag{35}$$

In Eq. (35), all the multipliers $f_{p,jk}/f^*_{jk}$ related to the j-th row and the k-th column of the matrices are divided by their average value. In case of perfect proportionality, all the values of λ_{jk} are equal to 1, so that it is possible to assume that a scalar value $\lambda^* = \frac{R^2}{\sum_{j=1}^{R} \sum_{k=1}^{R} \left(f_{p,jk} / f^*_{jk} \right)}$ exists, so that $\boldsymbol{F}^* = \lambda^* \boldsymbol{F_p}$; on the contrary, the more the values differ from unity, the less is the degree of proportionality between $\boldsymbol{F}^*$ and $\boldsymbol{F_p}$.

Figure 10 presents all the values that λ_{jk} assumes for all the considered damping models. It is evident that, for Case 1 (i.e., damping ratios that are equal for all the modes), the λ_{jk} multipliers are substantially all equal to 1, confirming the almost perfect proportionality between the two matrices. The results for Cases 4 and 5 show that, for the chosen models of both mass and stiffness proportional damping, the PFR matrix has a good level of proportionality with respect to the MF matrix (in Case 4, the values of λ_{jk} are mostly unit valued, with only one exception; in Case 5, all the values are between 0.7 and 1.3). Damping models used in Cases 2 and 3 are the ones that result in the lowest level of proportionality among the considered cases. This is expected because the two cases are the extreme theoretical cases (i.e., only mass- and only stiffness-proportional damping), and it has already been observed that the

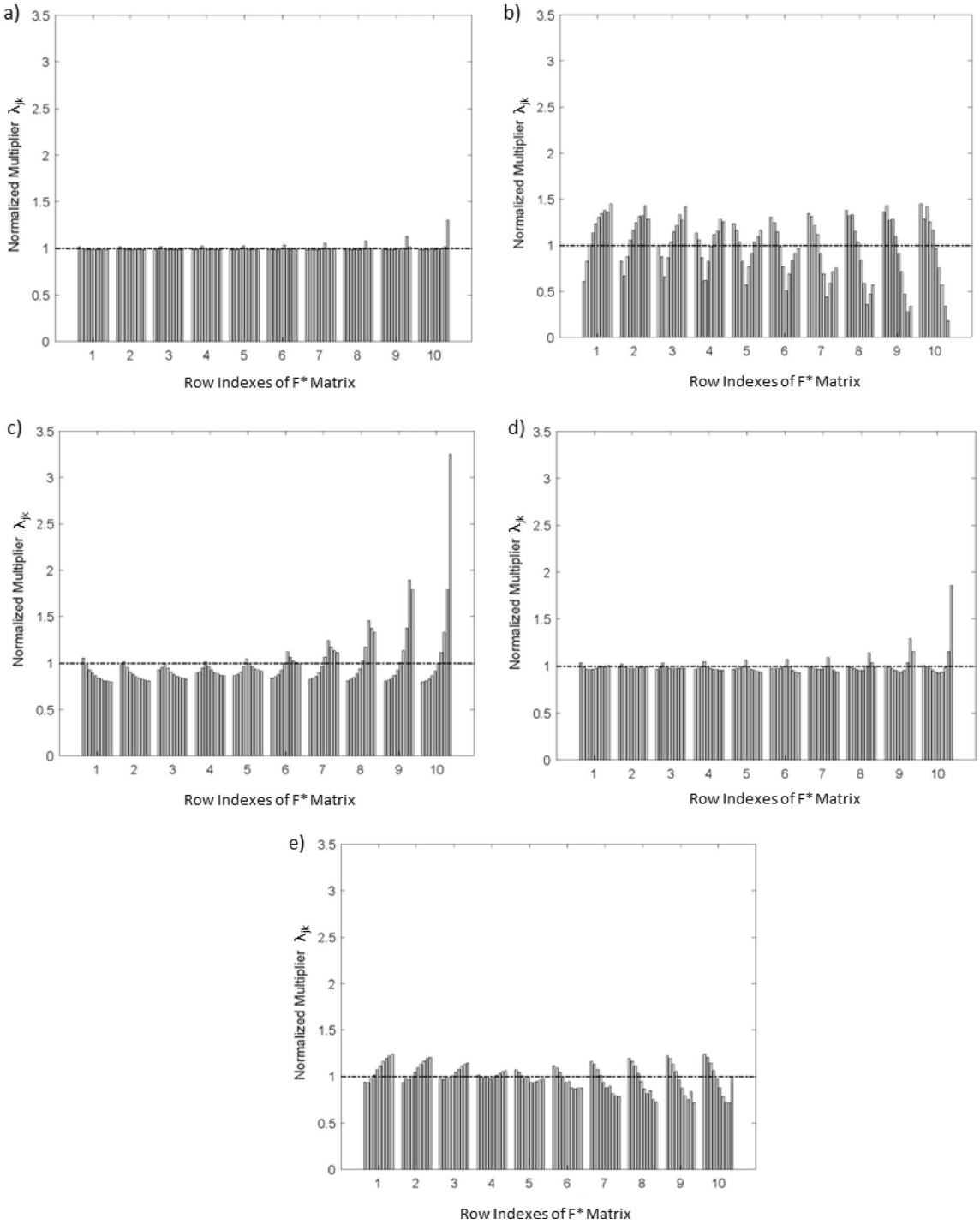

Fig. 10 Normalized multipliers between the PFR matrix and the MF matrix; results for five different models of damping: **a** case 1; **b** case 2; **c** case 3; **d** case 4; **e** case 5

corresponding values of γ that minimize the norm of the difference matrix $\Delta \boldsymbol{F}(\gamma)$ are $\gamma = 4$ and $\gamma = 2$, respectively.

This section has shown that the chosen formulation of the PFR matrix is the one that minimizes the discrepancies with respect to the modal flexibility matrix. The next section will show that, regardless of the considered damping model, the PFR matrix can be taken as a reliable tool to implement in damage detection strategies.

Table 3 Configurations used in the numerical simulation for damage localization (10-story shear building)

State	Condition	Description
1	Undamaged	Baseline
2	Damaged	30% stiffness reduction in the columns of the 6th interstory
3	Damaged	30% stiffness reduction in the columns of the 2nd interstory and 15% stiffness reduction in the columns of the 7th interstory

7 Verification of the effectiveness of the PFR matrix for damage localization

7.1 Application using simulated data

7.1.1 Shear building structure

The damage localization procedure based on the PFR matrix (Sect. 4) was tested through numerical simulations performed using the 10-story shear-type building structure described in Sect. 6. All the five damping models presented in the previous section were considered, to evaluate how the damage detection algorithm works in different and unknown damping scenarios.

The PFR matrix was calculated for the three structural configurations that are reported in Table 3. State 1 is the original configuration of the structure, and it represents an undamaged condition. In States 2 and 3 damage was introduced as localized stiffness reductions: in State 2 the damage was imposed at the 6th interstory of the shear building (30% story stiffness reduction), while in State 3 a multiple damage was imposed at the 2nd and 7th interstory (30% and 15% story stiffness reduction, respectively). For each state, the structure was excited by white noise inputs at all the DOFs, and the output was recorded in terms of displacement (this way, the cutoff frequency is $\widehat{\omega} = \Delta\omega$). The chosen sample frequency is $f_s = 64$Hz, with total duration of the signals equal to $T = 1920s$. Once the structural responses have been collected, the signal was divided in $\vartheta = 30$ segments (this way, $T_\vartheta = 64s$), and a 5% Root Mean Square (RMS) additive Gaussian noise was applied. The process was repeated for each structural state and for each damping model.

Furthermore, the same damage detection strategy was implemented using the truncated MF matrix $\boldsymbol{F_p}$ in place of $\boldsymbol{F}^*$. This way, the procedure based on the proposed PFR matrix was compared to the one based on a traditional MF matrix assembled using a selected number of structural modes. Specifically, referring to the analyses presented in this section, $\boldsymbol{F_p}$ was constructed for each state of the structure using natural frequencies and mass-scaled mode shapes that were analytically obtained by solving the eigenvalue problem $\left(\boldsymbol{K} - \omega_r^2 \boldsymbol{M}\right)\boldsymbol{\psi_r} = 0$. Since only the first six natural frequencies of the structure in the baseline state are below the Nyquist frequency (so that only the first six modes will contribute to the assemblage of $\boldsymbol{F}^*$), the chosen truncation mode of $\boldsymbol{F_p}$ is the sixth mode (i.e., $p = 6$). This was done to make a proper comparison, in terms of modal contributions, between the two procedures based on the PFR and the MF matrices.

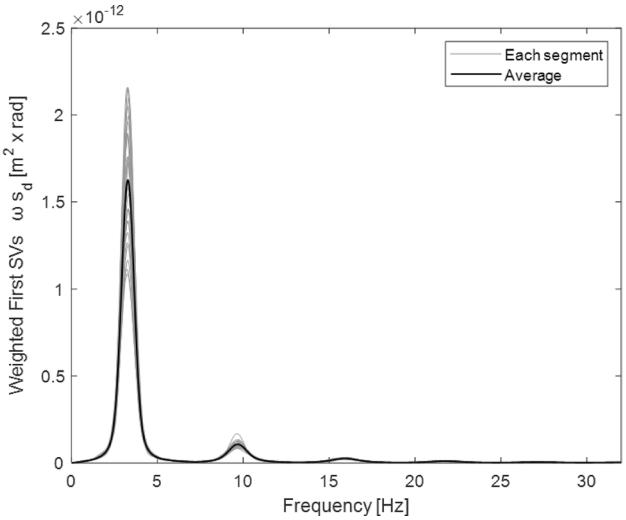

Fig. 11 Weighted first singular values—numerical simulation for damage localization (10 story shear building); baseline state for Case 1 (gray line: result for the single segments; black line: average values)

The weighted first singular values related to each k-th segment for State 1 and damping Case 1 are shown in Fig. 11, where the average is also reported. It appears that the maximum deviation from the average happens for frequencies that are close to the peaks, and that the deviation itself decreases when the mode order increases. Since the contribution to $\boldsymbol{F}^*$ of a generic mode is assumed to be proportional to the area underneath the corresponding averaged modal bell, it is evident that the modal contribution decreases rapidly with the mode order.

Figure 12 shows, for the considered baseline State 1 and the inspection States 2 and 3, the max-normalized deflections (δ_B and δ_I, respectively) and the story drifts (d_B and d_I). The quantities are normalized to their maximum value to ease the comparison. Overall, it must be noted that, for all the considered states, the deflections computed from $\boldsymbol{F}^*$ for damping Cases 1 and 4 almost perfectly superpose on the one obtained by $\boldsymbol{F_p}$; referring to story drifts, the three

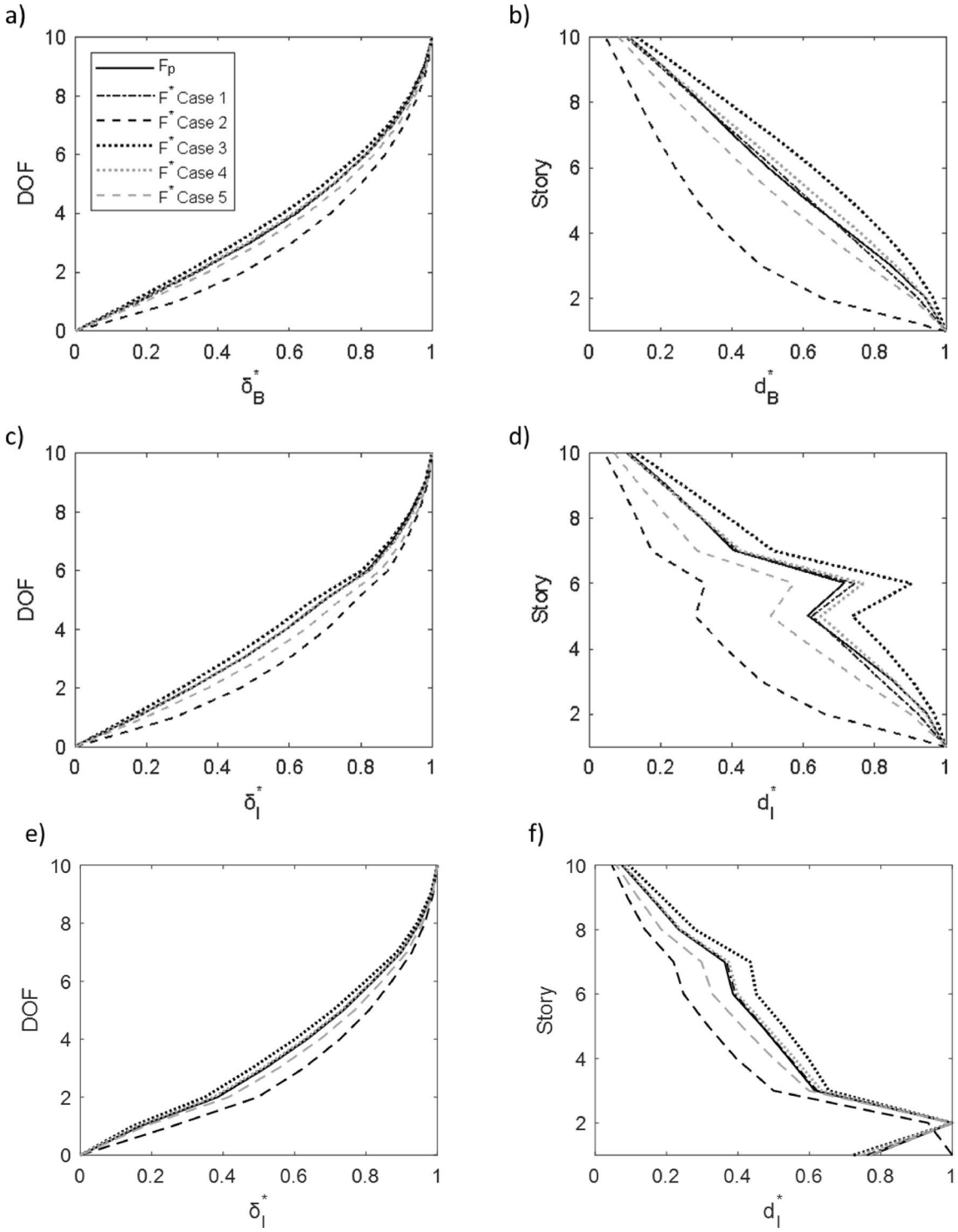

Fig. 12 Deflections and story drifts computed from the PFR matrix—numerical simulation for damage localization (10 story shear building; max-normalized values)—comparison between the approach based on the traditional modal flexibility matrix $\boldsymbol{F}_p$ and the approach based on the proposed PFR matrix $\boldsymbol{F}^*$: **a**, **b** state 1; **c**, **d** state 2; **e**, **f** state 3

diagrams are very close, confirming the high level of proportionality between the MF matrix and the PFR matrix for the mentioned damping models, as it has already been observed in Sect. 6. In all the diagrams, the quantities related to Case 5 place midway between the quantities from $\boldsymbol{F}_p$ and the quantities derived for Case 2. Cases 2 and 3 (i.e., only mass- and only stiffness-proportional damping, respectively) are again proven to be the extreme cases: for all considered

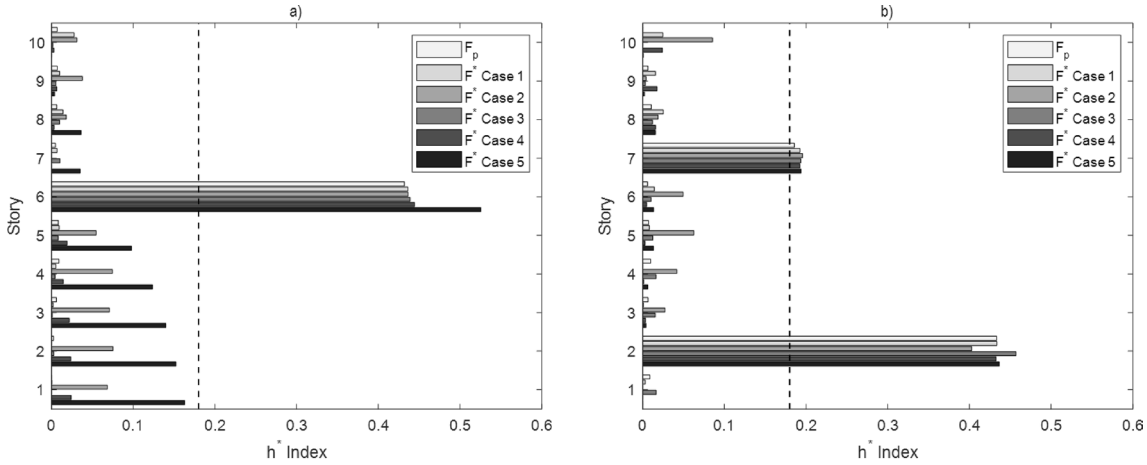

Fig. 13 Damage localization using the h^* index—numerical simulation for damage localization (10 story shear building)—comparison between the approach based on the traditional modal flexibility matrix $\boldsymbol{F_p}$ and the approach based on the proposed PFR matrix $\boldsymbol{F}^*$: **a** state 2; **b** state 3

states of the structure, Case 2 is the one that minimizes the story drifts, while Case 3 is the one that maximizes these quantities. Nevertheless, it is mostly important to notice that, by comparing story drift diagrams of State 1 and State 2, the drift of the sixth story increases for all the considered cases, altering the trends that characterize the baseline states, as an effect of the introduced damage. A similar pattern can be observed for the drifts at the 2nd and 7th stories (i.e., damaged stories) when comparing State 1 and State 3 for all the considered cases.

The damage localization technique was applied for both the inspection States 2 and 3, and the h_r^* index values are reported in Fig. 13 for all the considered cases. The dashed line represents the threshold h^{*TH}, which is equal to 0.18 and was set by repeating the procedure illustrated in Sect. 4 for all the considered damping cases. Overall, it must be noticed that the introduced damages are all localized using the proposed PFR matrix, with the damage index that exceeds the threshold at the corresponding damaged story. This result was obtained for both inspection states and for all the considered damping models. Furthermore, it can be observed in Fig. 13 that the values of the damage index at the damage stories obtained using the PFR matrix are comparable to those determined using the traditional MF matrix $\boldsymbol{F_p}$. It is, however, important to underline the differences in the procedures used for assembling the two matrices: while the natural frequencies and mass-scaled mode shapes of six structural modes were used to calculate the MF matrix, the proposed PFR matrix was assembled by processing all the

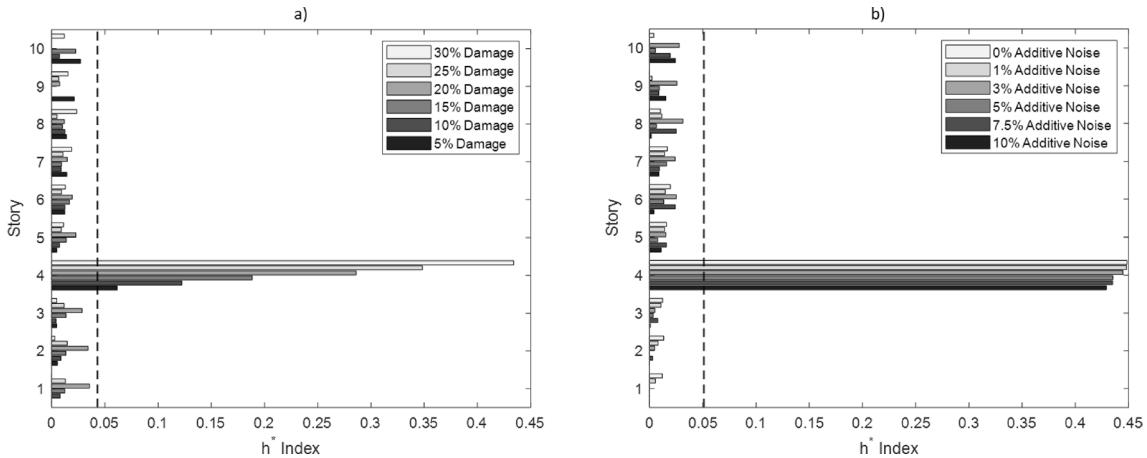

Fig. 14 Damage localization on the shear building model (case 1)—approach based on the proposed PFR matrix: **a** different scenarios with progressive damage and evaluation of the minimum detectable damage (5% additive noise); **b** scenarios with different levels of additive Gaussian noise (RMS values) applied on the structural responses (30% stiffness reduction imposed in the columns of the 4th interstory)

weighted first singular values shown in Fig. 11, together with the corresponding singular vectors.

A specific analysis was carried out to evaluate the minimum amount of damage for which a certain damaged story of the considered shear building structure can be identified using the proposed PFR matrix. For this analysis Case 1 was selected, and the analysis was performed under the same conditions of the analyses described in previous paragraphs (i.e., by considering the same signal length, the same sampling frequency, and the same amount of additive noise to be applied on the structural responses). Different scenarios with progressive damage were considered—i.e., increasing stiffness reductions imposed in the columns of the 4^{th} interstory of the structure. The results of this analysis are presented in Fig. 14a. As shown in the figure, the minimum amount of story stiffness reduction that leads to a correct damage localization is equal to a story stiffness reduction of 5%. Such value is comparable to the values of minimum detectable damage severity that were obtained in previous studies where the original existing PSIL method or variants of the same method were applied [30, 31]. In Fig. 14a, it can also be observed that the h_r^* index values at the damaged story progressively increase when considering the different scenarios with increasing amounts of the imposed damage. The analyses for the evaluation of the minimum amount of detectable damage were repeated by imposing stiffness reductions in different interstories of the structure (other than the 4^{th} interstory), and similar results were obtained.

To investigate how the results are affected by the level of noise, the damage localization process through the proposed PFR matrix was repeated by considering different RMS levels of additive noise to be applied on the structural responses of the shear building structure. The selected RMS levels of additive noise are: 0%, 1%, 3%, 5%, 7.5%, and 10%. For this analysis, Case 1 was selected, and the analysis was performed under the same conditions of the analyses described in previous paragraphs (i.e., by considering the same signal length and the same sampling frequency). In this analysis, a 30% stiffness reduction was imposed in the columns of the 4th interstory of the structure. The results of this analysis are presented in Fig. 14b, where the threshold $h^{*TH} = 0.051$ (dashed line) was set by repeating the procedure illustrated in Sect. 4 for all the considered levels of additive noise. As shown in the figure, no substantial differences in the values of the h_r^* index and a correct damage localization were observed for all the different levels of additive noise.

7.1.2 Beam-like structure

The damage localization procedure based on the proposed PFR matrix was also tested through numerical simulations on a flexure-type beam-like structure. The 10-DOF simply-supported beam described in Sect. 6 was selected for this purpose, thus its curvature was assumed to be the damage-sensitive feature. For this analysis, the first damping model (case 1) presented in the previous sections was considered (i.e., modal damping is constant over the different modes of the structure). The PFR matrix was calculated for two structural configurations. Namely, the Baseline State is the original configuration of the structure and represents an undamaged condition, while damage was introduced in the Inspection State as localized 30% stiffness reduction between the 2nd and the 3rd mass. In both the states, the structure was excited by white noise inputs at all the DOFs, while the response was recorded in terms of displacement for a duration $T = 1920s$, with sample frequency $f_s = 64Hz$. Once the structural responses have been collected, the signal was subsequently divided in $\vartheta = 30$ segments (this way, $T_\vartheta = 64s$), and a 5% RMS additive Gaussian noise was applied.

The weighted first singular values related to each k-th segment for the Baseline State, as well as their average, are reported in Fig. 15. As already observed for the shear building structure, the maximum deviation from the average happens for frequencies that are close to the peaks.

Figure 16 shows, for both the considered Baseline State and the Inspection State, the max-normalized deflections (δ_B^*

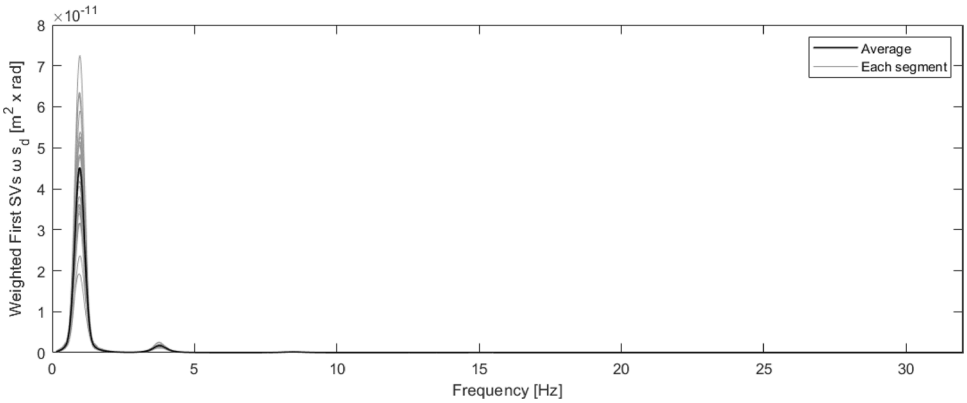

Fig. 15 Weighted first singular values—numerical simulation for damage localization (simply-supported beam modeled using 10 DOFs); baseline state for Case 1 (gray line: result for the single segments; black line: average values)

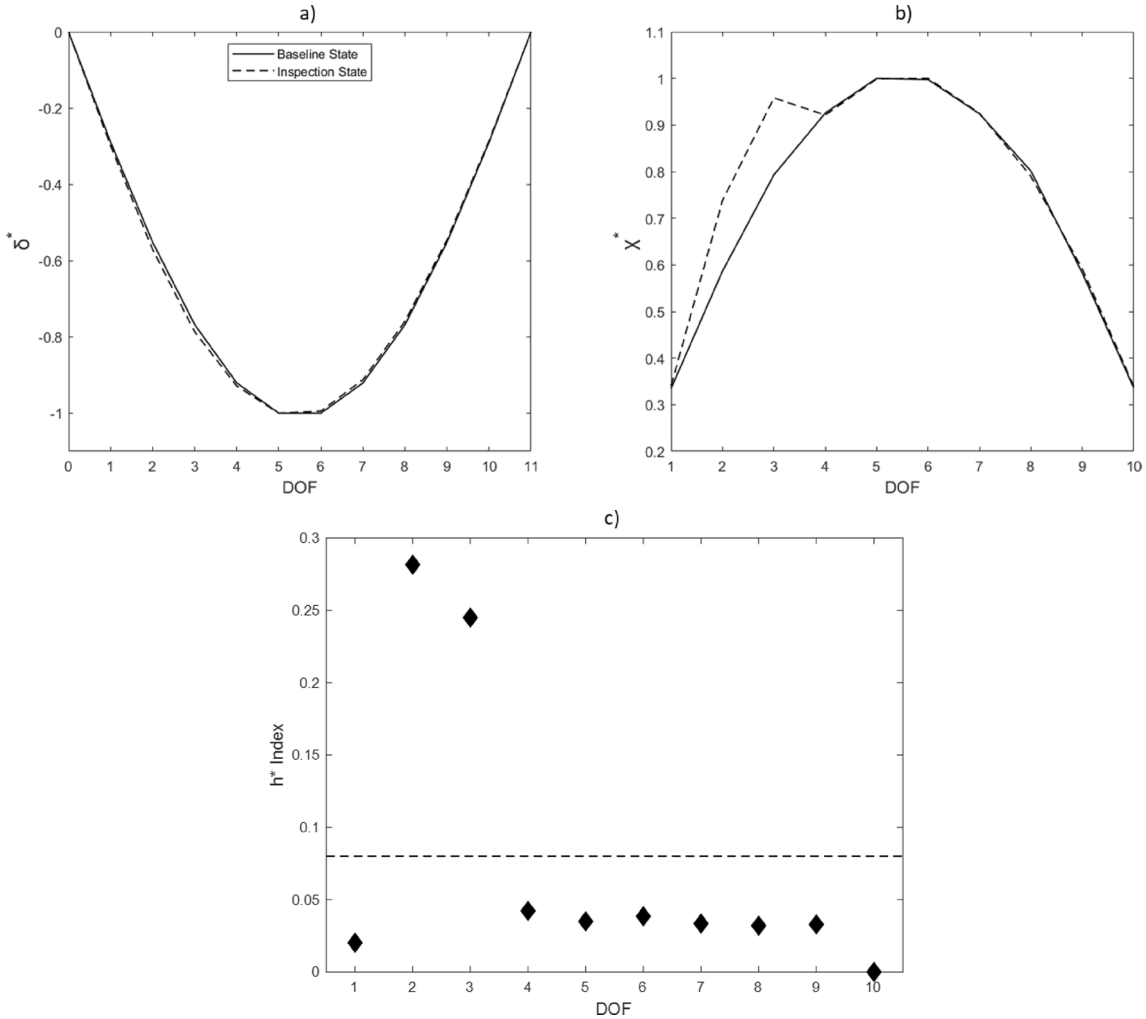

Fig. 16 Damage localization on the 10 DOF simply-supported beam—approach based on the proposed PFR matrix (numerical simulation): **a** deflections; **b** curvatures; **c** h^* index

and δ_I^*, Fig. 16a) and the max-normalized curvatures (χ_B^* and χ_I^*, Fig. 16b). Overall, it appears that the deflection shapes are almost perfectly superposed, while the presence of damage becomes evident while comparing χ_B^* and χ_I^*. In fact, the calculated curvature in the 2nd and 3rd DOFs strongly increases for the Inspection State, indicating a decrease in the flexural stiffness of the structure in the portions that are adjacent to these two DOFs. The obtained h_r^* index values are reported in Fig. 16c, where the dashed line represents the threshold $h^{*TH} = 0.08$. It is evident that the damage index exceeds the threshold for the 2nd and 3rd DOFs only, correctly detecting the presence of damage which was imposed in the portion of the structure between the aforementioned DOFs.

7.2 Application using experimental data

The damage localization procedure based on the PFR matrix (Sect. 4) was also applied using the datasets of experimental tests performed on a laboratory three-story frame structure (Figs. 17 and 18) [38, 39]. This frame structure is made of aluminum and is composed of columns and plates, assembled through bolted connections. The columns have a rectangular cross-section with dimensions 2.5×0.6 cm, while the thickness of the plates is 2.5 cm. The structure is supported on a baseplate with rails, and the sliding between the structure and the baseplate is allowed in the x direction only. Including the base floor that slides on the rails, the structure can thus be considered as a four degree-of-freedom system.

In the experimental tests, the input excitation was provided in the centerline of the base floor through an electrodynamic shaker, while the response of the structure was measured by four accelerometers positioned in the centerline

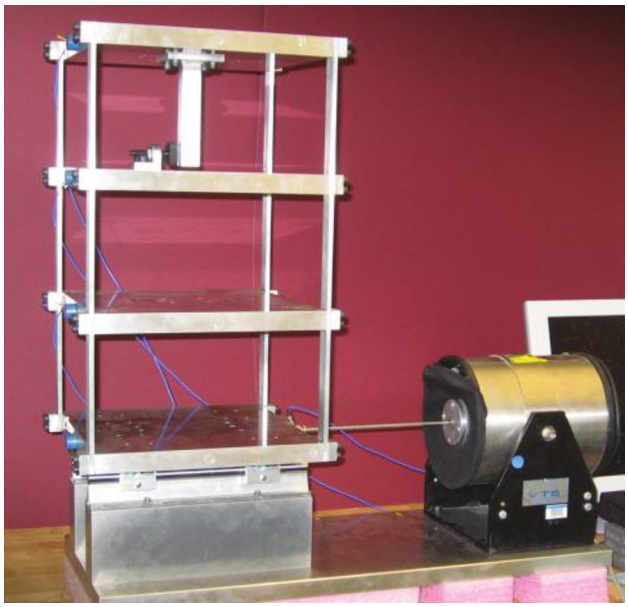

Fig. 17 Three-story testbed structure [38, 39]

of each floor, on the opposite side from the shaker. The used sampling frequency was 320 Hz, and the input provided by the shaker was a band-limited random excitation in the range 20–150 Hz. As stated in [38, 39], this range was selected to avoid the rigid body modes of the structure present below 20 Hz. The modal parameters of the structure were estimated in [38] using the rational-fraction polynomial method. As shown in [38], the natural frequencies of the first three modes (excluding the rigid body modes) are 30.7 Hz, 54.2 Hz, 70.7 Hz, while the modal damping ratios that correspond to these modes are 6.3%, 2.0%, 0.97%, respectively. For a more detailed description of the structure and the performed vibration tests, the reader is referred to [38, 39].

Only the output responses of the structure were considered in the analyses of the present paper. Moreover, four structural configurations related to the performed tests were used to apply the damage detection procedure, and these configurations are described in Table 4. On one side, configuration 1 is the original configuration of the structure, and it represents the baseline or "healthy" condition. On the other side, stiffness modifications were introduced in configurations 2–4, and these configurations represent the damaged conditions. Specifically, story stiffness reductions were imposed by replacing two columns with other columns with a reduced cross section. Compared to the original columns, the modified columns are characterized by a 50% reduction in the cross-sectional thickness in x direction (which is the direction of the excitation induced by the shaker). In configurations 2, 3, and 4 these modifications were introduced at the 1st, 2nd, and 3rd interstory, respectively. As highlighted in [38, 39], a 50% reduction in the thickness of one column corresponds to an 87.5% reduction in the stiffness of such a column. Overall, considering that two out of the four columns present at each story were replaced, the introduced modifications resulted in an approximately 43.8% reduction in the story stiffness in the direction of the applied base excitation.

In the analyses, the acceleration recorded at the base floor (i.e., channel 2 according to Fig. 18) was subtracted from the acceleration measured at the other floors, to obtain relative measurements. The length of the signals that were used to estimate the proposed PFR matrix was equal to $T = \vartheta T_\vartheta = 51.2s$, where $\vartheta = 8$ and $T_\vartheta = 6.4s$. The selected cutoff frequency was $\widehat{\omega} = 78.5\text{rad/s}$, which correspond to 12.5 Hz. The total length of the measurements related to the training dataset was equal to $LT = 1280s$, where $L = 25$; the calculated damage index threshold was $h^{*TH} = 0.6$.

Figure 19 shows the weighted first singular values related to the baseline state and to all the considered signal segments. The average values are also shown in the figure. It is evident that the modal bells of the first and the second mode have similar amplitudes: this implies that the modal contribution ratio ρ_{12} is close to unity, marking the fact that the first two modes will give almost the same contribution to $\boldsymbol{F}^*$. This fact is expected, since, according to the results that are shown in [38], the first modal damping ratio (i.e., 6.3%) is more than three times higher than the second (i.e., 2%).

The damage localization strategy presented in Sect. 4 was applied, considering both the undamaged and the damaged conditions of the structure as inspection states. In Fig. 20, the damage indexes h_r^* are reported for all the four configurations of Table 4. Figure 20a shows the resulting indexes of the case where the structure related to the inspection phase is undamaged and equal to the baseline structure. It is clearly shown that h_r^* does not exceed the threshold (represented with the dashed line) for any of the measured stories. Figure 20b–d show the indexes that were extracted for the other three states: it is possible to observe that the index h_r^* exceeds the threshold h^{*TH} only at the actually damaged stories, thus proving that the damage localization based on the proposed PFR matrix has been performed correctly.

8 Conclusions

This paper proposes a method for estimating a proportional flexibility-resembling matrix. Such a matrix can be estimated for structures subjected to output-only vibration tests, and it is shown in the paper that this matrix can be used for damage detection and localization purposes. The PFR matrix is obtained through signal processing operations to be executed after applying the first steps of the Frequency-Domain Decomposition technique—i.e., after the singular value decomposition of the spectral density matrix. The

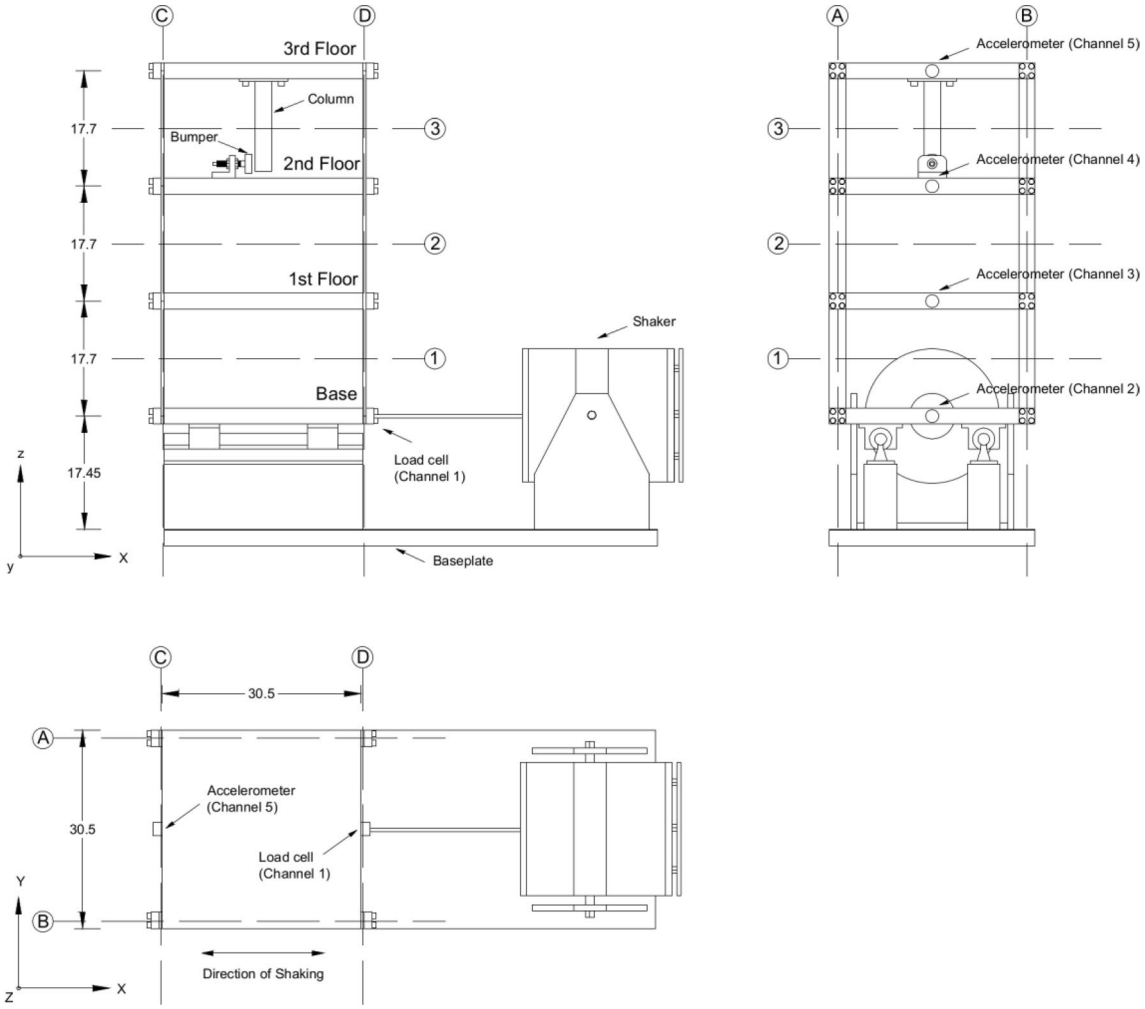

Fig. 18 Three-story testbed structure: geometry and locations of the sensors (dimensions in cm) [38, 39]

Table 4 Configurations related to the experimental test and used for damage localization (three-story testbed structure)

State	Condition	Description
1	Undamaged	Baseline
2	Damaged	Two columns at the 1st interstory with a 50% reduction in the cross-sectional thickness in *x* direction
3	Damaged	Two columns at the 2nd interstory with a 50% reduction in the cross-sectional thickness in x direction
4	Damaged	Two columns at the 3rd interstory with a 50% reduction in the cross-sectional thickness in *x* direction

defining aspect of the PFR matrix is that, differently from the traditional formulation of modal flexibility and proportional flexibility matrices, it can be assembled without the need of an explicit identification of the modal parameters of the structure. In fact, the PFR matrix is estimated by processing all first singular vectors and all first singular values in a selected frequency range. The PFR matrix can be equally obtained from displacement, velocity or acceleration responses, and specific measures have been introduced in the method to avoid the amplification of the noise that typically occurs at the frequencies close to DC when integrating time signals in frequency domain.

The calibration of the procedure used to weigh the first singular values through the corresponding angular frequencies represented a fundamental step in the definition of the PFR matrix. Such a procedure is crucial to guarantee that the contribution in the PFR matrix of the weighted singular values that belong to a particular mode frequency band is similar to the contribution of the corresponding mode in the traditional flexibility matrix. As shown in Sect. 6, the

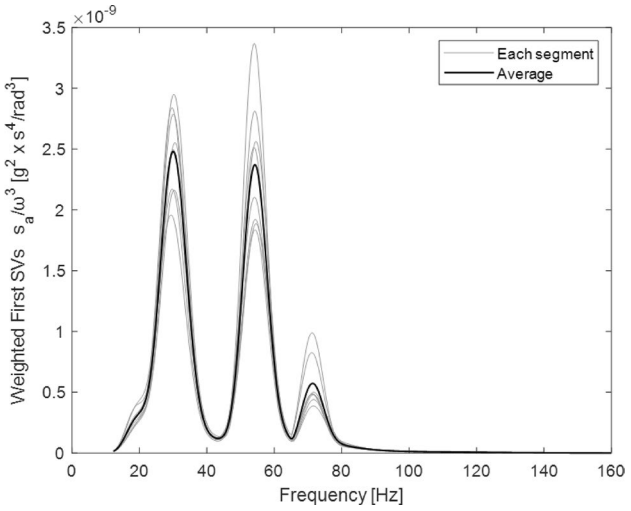

Fig. 19 Weighted first singular values; baseline state (state 1) of the three-story testbed structure; gray line: result for the single segments; black line: average values

mentioned calibration was performed through parametric studies executed for different structural models (i.e., shear building, simply supported beam, and cantilever beam models), and by defining specific indicators able to quantify the level of resemblance between the proposed PFR matrix and the traditional flexibility matrix. The analyses also revealed that the contribution in the PFR matrix of the weighted singular values that belong to a particular mode frequency band is affected by the damping properties. Moreover, the analyses showed that the highest level of resemblance between the PFR matrix and the traditional flexibility matrix is obtained in the case of modal damping ratios that are constant for all the modes. Based on these observations, structures with different types of damping models were considered in the mentioned parametric analyses, including cases of both uniform and non-uniform modal damping ratios. These analyses showed that, overall, the selected procedure for obtaining the weighted singular values is the one that minimizes the discrepancies between the proposed proportional flexibility-resembling matrix and the traditional flexibility matrix.

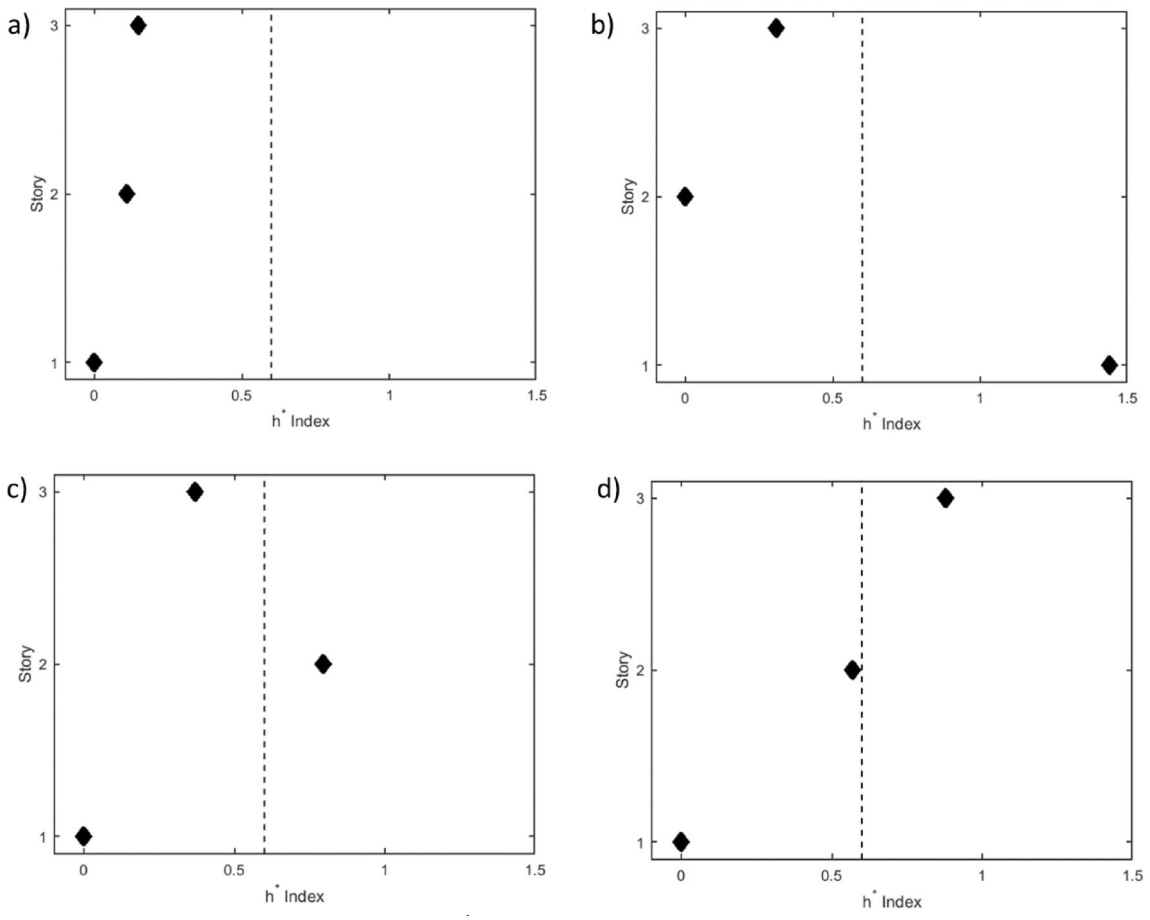

Fig. 20 Damage localization using the h^* index—approach based on the proposed PFR matrix (three-story testbed structure): **a** state 1; **b** state 2; **c** state 3; **d** state 4

To show that the proposed PFR matrix can be used for damage detection purposes, existing flexibility-based damage detection methods developed for shear building structures and flexure-type beam-like structures have been considered, and the proposed PFR matrix has been used in place of the traditional flexibility matrix. Referring to shear building structures, the resulting damage detection method was tested both through numerical simulations performed on a 10-story shear building model and using the experimental data of vibration tests that were executed on a laboratory three-story frame structure. In both cases and for the different damage scenarios that were considered (for example, either single or multiple damage scenarios), the performed analyses showed the ability of the used method, based on the PFR matrix, to detect the stories of the structure that have been affected by the damage. This result of a correct localization of the damage was obtained for all the considered structures, including structures with different types of damping models and the general case of non-uniform modal damping ratios associated to the different modes. Referring to flexure-type beam-like structures, numerical simulations performed on a simply-supported beam modeled using 10 DOFs showed the applicability and effectiveness of the proposed PFR matrix for localizing damage in this type of structures.

In future research an attempt could be made to develop an enhanced version of the PFR matrix estimation procedure, with the objective of understanding if the estimates of such a matrix can be further improved in the case of non-uniform modal damping ratios. One potential option that could be examined is to include the identification of the damping properties in the PFR matrix estimation procedure. This, however, will surely lead to a more complex procedure, and it has to be carefully evaluated if, for the case of non-uniform modal damping ratios, this increased complexity is appropriately justified by a potential further improvement in the accuracy of the estimated proportional flexibility-resembling matrix.

Appendix A: Modal contribution in the flexibility matrix

This appendix shows how Eq. (23) was derived. Starting from Eqs. (1,2), the portion of the modal flexibility matrix that is due to a single mode is expressed as follows:

$$\boldsymbol{F}_{(r)} = \frac{\boldsymbol{\phi}_r \boldsymbol{\phi}_r^T}{\omega_r^2} = \frac{\boldsymbol{\psi}_r \boldsymbol{\psi}_r^T}{\mu_r \omega_r^2} \tag{A1}$$

where the r-th mode has been considered. The overall contribution to the flexibility matrix of this r-th mode is evaluated herein by applying the Frobenius norm to the matrix $\boldsymbol{F}_{(r)}$, where for a generic $m \times n$ matrix $\boldsymbol{A}$ the Frobenius norm is $\|\boldsymbol{A}\|_F = \sqrt{\sum_{i=1}^{m}\sum_{j=1}^{n}\left|a_{ij}\right|^2}$. Specifically, it can be demonstrated that the Frobenius norm of the matrix $\boldsymbol{F}_{(r)}$ is equal to the following expression:

$$\|\boldsymbol{F}_{(r)}\|_F = \frac{\|\boldsymbol{\psi}_r\|_2^2}{\mu_r \omega_r^2} \tag{A2}$$

where $\|\bullet\|_2$ is the Euclidean norm operator to be applied on a generic vector. Eq. (A2) is valid because the generic r-th mode shape vector satisfies the following relationship $\|\boldsymbol{\psi}_r \boldsymbol{\psi}_r^T\|_F = \|\boldsymbol{\psi}_r\|_2^2$, and this last expression can be derived by considering the following property of the Frobenius norm: $\|\boldsymbol{A}\|_F = \sqrt{tr(\boldsymbol{A}\boldsymbol{A}^T)}$, where $tr(\bullet)$ denotes the trace operator (i.e., for a square matrix the trace is the sum of the elements of the main diagonal).

Using the Frobenius norm and Eq. (A2), the contribution ratio in the modal flexibility matrix between two generic modes (i.e., the r-th and the s-th mode) can thus be expressed as:

$$\xi_{rs} = \frac{\|\boldsymbol{F}_{(r)}\|_F}{\|\boldsymbol{F}_{(s)}\|_F} = \frac{\|\boldsymbol{\psi}_r\|_2^2 \mu_s \omega_s^2}{\|\boldsymbol{\psi}_s\|_2^2 \mu_r \omega_r^2} \tag{A3}$$

If the considered structure has a perfectly regular distribution of masses, such that the diagonal mass matrix $\boldsymbol{M}$ has values that are all equal to m (i.e., $\boldsymbol{M} = m\boldsymbol{I}$, where $\boldsymbol{I}$ is the identity matrix), it can be demonstrated that the contribution ratio of Eq. (A3) depends only on the angular frequency squared, as shown in Eq. (23).

Acknowledgements The use of the data of the experimental tests performed on the three-story building structure at the Engineering Institute at Los Alamos National Laboratory is gratefully acknowledged.

Author contributions Conceptualization: AC, GB, SC, LL, PPD. Investigation: AC, GB. Methodology: AC, GB. Software: AC. Supervision: SC, LL, PPD. Visualization: AC, GB. Writing—original draft: AC, GB. Writing—review & editing: SC, LL, PPD.

Funding Open access funding provided by Alma Mater Studiorum - Università di Bologna within the CRUI-CARE Agreement. For conducting this study, no funding was received outside of the primary affiliations of the authors.

Data availability The data of the experimental tests performed on the three-story building structure at the Engineering Institute at Los Alamos National Laboratory were used in this paper. The data of these tests were made available to the public domain at http://institute.lanl.gov/ei/software-and-data/ and are also available for download at https://www.lanl.gov/projects/national-security-education-center/engineering/software/shm-data-sets-and-software.php.

Declarations

Conflict of interest The authors declare that they have no known competing financial interests or personal relationships that could have appeared to influence the work reported in this paper.

References

1. Brincker R, Ventura C (2015) Introduction to operational modal analysis, 1st edn. Wiley, Chichester
2. Rainieri C, Fabbrocino G (2014) Operational modal analysis of civil engineering structures. Springer, New York
3. Farrar R, Worden K (2013) Structural health monitoring: a machine learning perspective, 1st edn. Wiley, Chichester
4. Brincker R, Zhang L, Andersen P (2001) Modal identification of output-only systems using frequency domain decomposition. Smart Mater Struct 10(3):441–445. https://doi.org/10.1088/0964-1726/10/3/303
5. Brincker R, Andersen P (2004) Method for vibration analysis. United States patent no. US 6779404 B1
6. Li S, Wu Z (2008) A model-free method for damage locating and quantifying in a beam-like structure based on dynamic distributed strain measurements. Comput-Aided Civ Infrastruct Eng 23(5):404–413. https://doi.org/10.1111/j.1467-8667.2008.00545.x
7. Sohn H, Kim SD, Harries K (2008) Reference-free damage classification based on cluster analysis. Comput-Aided Civ Infrastruct Eng 23(5):324–338. https://doi.org/10.1111/j.1467-8667.2008.00541.x
8. Pai PF (2013) Time-frequency analysis for parametric and nonparametric identification of nonlinear dynamical systems. Mech Syst Signal Process 36(2):332–353. https://doi.org/10.1016/j.ymssp.2012.12.002
9. Liu L, Zhang X, Lei Y (2023) Data-driven identification of structural damage under unknown seismic excitations using the energy integrals of strain signals transformed from transmissibility functions. J Sound Vib 546:117490. https://doi.org/10.1016/j.jsv.2022.117490
10. Pandey AK, Biswas M (1994) Damage detection in structures using changes in flexibility. J Sound Vib 169(1):3–17. https://doi.org/10.1006/jsvi.1994.1002
11. Bernagozzi G, Quqa S, Landi L, Diotallevi PP (2022) Structure-type classification and flexibility-based detection of earthquake-induced damage in full-scale RC buildings. J Civil Struct Health Monit 12:1443–1468. https://doi.org/10.1007/s13349-022-00584-2
12. Koo KY, Lee JJ, Yun CB, Kim JT (2008) Damage detection in beam-like structures using deflections obtained by modal flexibility matrices. Smart Struct Syst 4(5):605–628. https://doi.org/10.12989/sss.2008.4.5.605
13. Catbas FN, Brown DL, Aktan AE (2006) Use of modal flexibility for damage detection and condition assessment: case studies and demonstrations on large structures. J Struct Eng 132(11):1699–1712. https://doi.org/10.1061/(ASCE)0733-9445(2006)132:11(1699)
14. Gul M, Catbas FN (2008) Ambient vibration data analysis for structural identification and global condition assessment. J Eng Mech 134(8):650–662. https://doi.org/10.1061/(ASCE)0733-9399(2008)134:8(650)
15. Koo KY, Sung SH, Park JW, Jung HJ (2010) Damage detection of shear buildings using deflections obtained by modal flexibility. Smart Mater Struct 19(11):115026. https://doi.org/10.1088/0964-1726/19/11/115026
16. Bernagozzi G, Mukhopadhyay S, Betti R, Landi L, Diotallevi PP (2018) Output-only damage detection in buildings using proportional modal flexibility-based deflections in unknown mass scenarios. Eng Struct 167:549–566. https://doi.org/10.1016/j.engstruct.2018.04.036
17. Bernagozzi G, Mukhopadhyay S, Betti R, Landi L, Diotallevi PP (2022) Proportional flexibility-based damage detection for buildings in unknown mass scenarios: the case of severely truncated modal spaces. Eng Struct 259:114145. https://doi.org/10.1016/j.engstruct.2022.114145
18. Duan Z, Yan G, Ou J, Spencer BF (2005) Damage localization in ambient vibration by constructing proportional flexibility matrix. J Sound Vib 284:455–466. https://doi.org/10.1016/j.jsv.2004.06.046
19. Li J, Baisheng Wu, Zeng QC, Lim CW (2010) A generalized flexibility matrix based approach for structural damage detection. J Sound Vib 329:4583–4587. https://doi.org/10.1016/j.jsv.2010.05.024
20. Bernagozzi G, Landi L, Diotallevi PP (2017) Truncation error analysis on modal flexibility-based deflections: application to mass regular and irregular structures. Eng Struct 142:192–210. https://doi.org/10.1016/j.engstruct.2017.03.057
21. Bernal D (2001) A subspace approach for the localization of damage in stochastic systems. In: Chang FK (ed) Structural health monitoring: the demand and challenges—proceedings of the 3rd international workshop in structural health monitoring. CRC Press, Boca Raton, pp 899–908
22. Duan Z, Yan G, Ou J, Spencer BF (2007) Damage detection in ambient vibration using proportional flexibility matrix with incomplete measured DOFs. Struct Control Health Monit 14(2):186–196. https://doi.org/10.1002/stc.149
23. Quqa S, Landi L, Diotallevi PP (2018) On the use of singular vectors for the flexibility-based damage detection under the assumption of unknown structural masses. Shock Vib. https://doi.org/10.1155/2018/9837694
24. Park HJ, Koo KY, Yun CB (2007) Modal flexibility-based damage detection technique of steel beam by dynamic strain measurements using FBG sensors. Steel Struct 7:11–18
25. Aulakh DS, Bhalla S (2023) Piezo sensor based multiple damage detection under output only structural identification using strain modal flexibility. Mech Syst Signal Process 194:110272. https://doi.org/10.1016/j.ymssp.2023.110272
26. Wang F, Li R, Xiao Y, Deng Q, Li X, Song X (2021) A strain modal flexibility method to multiple slight damage localization combined with a data fusion technique. Measurement 182:109647. https://doi.org/10.1016/j.measurement.2021.109647
27. Gao Y, Spencer BF Jr, Bernal D (2007) Experimental verification of the flexibility-based damage locating vector method. J Eng

Mech 133(10):1043–1049. https://doi.org/10.1061/(ASCE)0733-9399(2007)133:10(1043)
28. Catbas FN, Gul M, Burkett JL (2008) Damage assessment using flexibility and flexibility-based curvature for structural health monitoring. Smart Mater Struct 17(1):015024. https://doi.org/10.1088/0964-1726/17/01/015024
29. Sung SH, Jung HJ, Jung HY (2013) Damage detection for beam-like structures using the normalized curvature of a uniform load surface. J Sound Vib 332(6):1501–1519. https://doi.org/10.1016/j.jsv.2012.11.016
30. Sung SH, Koo KY, Jung HY, Jung HJ (2012) Damage-induced deflection approach for damage localization and quantification of shear buildings: validation on a full-scale shear building. Smart Mater Struct 21(11):115013. https://doi.org/10.1088/0964-1726/21/11/115013
31. Bernagozzi G, Ventura CE, Allahdadian S, Kaya Y, Landi L, Diotallevi PP (2020) Output-only damage diagnosis for plan-symmetric buildings with asymmetric damage using modal flexibility-based deflections. Eng Struct 207:110015. https://doi.org/10.1016/j.engstruct.2019.110015
32. López-Aenlle M, Fernández P, Brincker R, Fernández-Canteli A (2010) Scaling-factor estimation using an optimized mass-change strategy. Mech Syst Signal Process 24(5):1260–1273. https://doi.org/10.1016/j.ymssp.2009.06.011
33. Aenlle ML, Brincker R (2013) Modal scaling in operational modal analysis using a finite element model. Int J Mech Sci 76:86–101. https://doi.org/10.1016/j.ijmecsci.2013.09.003
34. Alvin FK, Robertson AN, Reich GW, Park KC (2003) Structural system identification: from reality to model. Comput Struct 81:1149–1176. https://doi.org/10.1016/S0045-7949(03)00034-8
35. Castellaro S, Isani S (2019) Experimental modal analysis of bridges: how to employ few resources and get it right. FastTIMES 24(3):78–83
36. Møller N, Gade S, Herlufsen H (2005) Stochastic subspace identification technique in operational modal analysis. In: 1st International Operational Modal Analysis Conference, April 26–27, Copenhagen, Denmark
37. Clough RW, Penzien J (1995) Dynamics of structures. Computers & Structures Inc, London
38. Figueiredo E, Park G, Figueiras J, Farrar CR, Worden K (2009) Structural health monitoring algorithm comparisons using standard datasets. Report LA-14393, Los Alamos National Laboratory, Los Alamos, NM, USA
39. Figueiredo E, Flynn E (2009) Three-story building structure to detect nonlinear effects. Report SHMTools data description, Los Alamos National Laboratory